

# Topological semimetals without quasiparticles

Haoyu Hu<sup>1</sup>, Lei Chen<sup>1</sup>, Chandan Setty<sup>1</sup>, Mikel Garcia-Diez<sup>2,3</sup>, Sarah E. Grefe<sup>4</sup>,  
Andrey Prokofiev<sup>5</sup>, Stefan Kirchner<sup>6,7</sup>, Maia G. Vergniory<sup>2,8</sup>, Silke Paschen<sup>5,1</sup>,  
Jennifer Cano<sup>9,10</sup>, and Qimiao Si<sup>1,\*</sup>

<sup>1</sup>*Department of Physics and Astronomy, Rice Center for Quantum Materials, Rice University, Houston, Texas, 77005, USA*

<sup>2</sup>*Donostia International Physics Center, P. Manuel de Lardizabal 4, 20018 Donostia-San Sebastian, Spain*

<sup>3</sup>*Department of Physics, University of the Basque Country (UPV-EHU), Bilbao, Spain*

<sup>4</sup>*Theoretical Division, Los Alamos National Laboratory, Los Alamos, New Mexico 87545, USA*

<sup>5</sup>*Institute of Solid State Physics, TU Wien, Wiedner Hauptstr. 8-10, 1040 Vienna, Austria*

<sup>6</sup>*Department of Electrophysics, National Yang Ming Chiao Tung University, Hsinchu 30010, Taiwan*

<sup>7</sup>*Center for Emergent Functional Matter Science, National Yang Ming Chiao Tung University, Hsinchu 30010, Taiwan*

<sup>8</sup>*Max Planck Institute for Chemical Physics of Solids, Noethnitzer Str. 40, 01187 Dresden, Germany*

<sup>9</sup>*Department of Physics and Astronomy, Stony Brook University, Stony Brook, NY 11794, USA*

<sup>10</sup>*Center for Computational Quantum Physics, Flatiron Institute, New York, NY 10010, USA*

The interplay between interactions and topology in quantum materials is of extensive current interest. Strong correlations are known to be important for insulating topological states, as exemplified by the fractional quantum Hall effect. For the metallic case, whether and how they can drive topological states that have no free-electron counterparts is an open and pressing question. We introduce a general framework for lattice symmetries to constrain single-particle excitations even when they are not quasiparticles, and substantiate it in a periodic Anderson model with two channels of conduction electrons. We demonstrate that symmetry constrains correlation-induced emergent excitations to produce non-Fermi liquid topological phases. The loss of quasiparticles in these phases is manifested in a non-Fermi liquid form of spectral and transport properties, whereas its topological nature is characterized by surface states and valley and spin Hall conductivities. We also identify candidate materials to realize the proposed phases. Our work opens a door to a variety of non-Fermi liquid topological phases in a broad range of strongly correlated materials.

States of matter and their transitions have traditionally been classified in terms of Landau's order-parameter framework, which is based on global symmetry and its spontaneous breaking (1). For free-electron systems, typically with large spin-orbit couplings, the topological paradigm distinguishes electronic states in terms of certain topological invariants associated with their quantum-mechanical wavefunctions (2). The electronic topology is responsible for various novel phenomena, such as unusual Hall effects and development of nontrivial surface states. In recent years, much progress has been made in realizing metallic topological phases, including those that harbor Weyl and Dirac fermions (3, 4). Crystalline symmetries play an important role in stabilizing such topological semimetals (5–10).

In metallic topological states, electron correlations are typically treated perturbatively (3, 4). The pursuit of strongly correlated topological semimetals is largely in its infancy (11, 12). Nonetheless, recent studies – both theoretical (13, 14) and experimental (15, 16) – have demonstrated that correlations drive composite fermions with highly renormalized topological nodal excitations that are pinned to the Fermi energy. An important ingredient in realizing the correlated topological semimetals is that strong correlations and space-group symmetry cooperate (17). As exemplified by the fractional quantum Hall effect (18), strong correlations can lead to insulating topological states that do not have noninteracting counterparts. In the metallic case, realizing such topological states represents an outstanding challenge.

Here we advance the notion that space-group symmetry constrains emergent (low-energy) electronic excitations, which are induced by strong correlations and particularly electron fractionalization, to produce non-Fermi liquid topological phases. Such phases lose Landau quasi-particles and have no free-electron counterpart. Figure 1A illustrates the idea.

We start by providing a general theoretical foundation for the lattice symmetries of interacting systems to constrain dispersive electronic excitations, even when they are no longer quasi-particles. The Green's functions describe the electronic (single-particle) excitations of an in-

interacting electron system. The Green's function matrix  $[G]$  can be expressed in terms of their eigenvectors,  $v_i(\omega, \mathbf{k})$ , and eigenfunctions (19); the imaginary part of the eigenfunctions corresponds to the spectral functions, with their peaks describing dispersive electronic excitations regardless of whether they are quasiparticles. Consider the action of an element,  $h$ , of the space group  $H$  on an electron annihilation operator  $\psi$  in the space of internal quantum numbers ( $a$ ), frequency ( $\omega$ ) and wave vector ( $\mathbf{k}$ ):

$$h \in H : \psi_{a,i\omega,\mathbf{k}} \rightarrow \sum_b [U_h^\dagger(\mathbf{k})]_{ab} \psi_{b,i\omega,h\mathbf{k}}, \quad (1)$$

where  $U_h(\mathbf{k})$  is a unitary matrix. It follows from symmetry that  $[\mathcal{U}_h v_i]_{(a,i\omega,\mathbf{k})}$  is also an eigenvector of  $[G]$ , where  $[\mathcal{U}_h]_{(a,i\omega,\mathbf{k}),(b,i\omega',\mathbf{k}')} = \delta_{\omega,\omega'} \delta_{\mathbf{k}',h\mathbf{k}} U_h(\mathbf{k})$ . [The details are described in the Supplementary Materials (SM), Sec. A.]

We therefore reach the important conclusion that the set of all eigenvectors  $\{v_i\}_{i=1,2,\dots}$  form a representation space of the space group  $H$ . This sets the stage to examine the dispersive modes through the subset of eigenvectors that form certain irreducible representations of the space group associated with a given wavevector  $\mathbf{k}$ , similarly as for the Bloch functions in the case of noninteracting electrons (10) (SM, Sec. A). As we tune the wavevector to some high symmetry points, where additional symmetry leads to a two or higher dimensional irreducible representation, the entire (frequency-dependent) spectral functions of the corresponding dispersive modes must be degenerate. The same conclusion is reached if, alternatively, as we continuously tune the wavevector, the peaks of two dispersive modes from two different irreducible representations cross; this node cannot be removed by symmetry preserving disruptions. As such, our procedure provides a robust route to correlated topological semimetals, including ones that cannot be adiabatically connected to free-electron systems.

We now turn to a proof-of-principle demonstration of this general framework in a well-defined model. Our focus is on a periodic Anderson model, in which correlated electrons act

as local moments that are coupled to two degenerate channels of conduction electrons. As illustrated in Fig. 1B, the local degrees of freedom at any given site correspond to a doublet in the ground state manifold, with (pseudo-)spins  $\sigma = \uparrow, \downarrow$ , which hybridizes with two channels of conduction electrons, labeled by  $\alpha = 1, 2$ , via an excited doublet. Two channels of Kondo couplings lead to frustration in the development of Kondo entanglement, providing a means of fractionalizing the electronic excitations (20–23). The model, thus, provides an ideal setting to explore lattice symmetry constraints on emergent excitations for non-Fermi liquid topology. Further details of the model and solution method are provided in the SM (Secs. B,C,D).

To address the symmetry constraints on emergent excitations, we choose to analyze the model in a three-dimensional (3D) kagome lattice, where the space group allows for protected nodes and, in addition, whose inversion symmetry breaking can be readily tuned (SM, Secs. B,C). Here,  $c_{i,\sigma,\alpha}$  ( $d_{i,\sigma,\alpha}$ ) denotes a conduction (local) electron, describing the physical *spd-* (*f-*) electron, on site  $i$ , which marks both the unit cell position and sub-lattice index. We solve the model within dynamical mean-field theory (DMFT) (24), while ensuring that our results capture the *asymptotically-exact*  $\sqrt{|\omega|}$  low-energy behavior in the multi-channel Kondo model (21, 25). The Green's function of the conduction electrons are calculated via  $G_c(\omega, \mathbf{k}) = [\omega - t_{\mathbf{k}} - \Sigma_c(\omega)]^{-1}$ . Here,  $t_{\mathbf{k}}$  is the hopping matrix, and  $\Sigma_c(\omega)$  is the local self-energy that encodes the correlation effects on the single-electron excitations. We solve the dynamical equations in real frequency and reach extremely low temperatures (compared to  $T_K$ , the Kondo temperature, which is the dynamically generated low-energy scale) (SM, Sec. D) in order to reveal the asymptotic low-energy behavior.

The imaginary part of the conduction-electron self-energy,  $\text{Im}\Sigma_c(\omega)$ , is found to depend on frequency in a square-root fashion in the low-energy limit (SM, Fig. S2A). The  $\sqrt{|\omega|}$  form ensures that the spectral width of any dispersive mode will become progressively larger than its energy on approach of the Fermi energy, in contrast to what happens when the electronic

excitations are quasiparticles. It describes a non-Fermi liquid, as characterized by an electrical resistivity that depends on temperature ( $T$ ) in a  $\sqrt{T}$  (SM, Fig. S2B). These asymptotic results are found only when our calculations are done at sufficiently low temperatures (SM, Sec. E). The asymptotic form of the self-energy, however, is not adequate: On its own, it would not lead to new dispersive modes near the Fermi energy. Importantly, we find that the self-energy is described by a pole in the complex energy plane, with relevant energy scales of the order  $T_K$ . This pole, in turn, gives rise to narrow bands that are pinned to the Fermi energy (Secs. E,F and Fig. S6). The results for the narrow bands are shown in Fig. 2A.

In the above sense, the dispersive modes near the Fermi energy are *emergent* electronic excitations. Crucially, they go beyond Landau quasiparticles: For reasons described earlier and as seen in Fig. 2A, any peak of the spectral function *vs.* energy for a given wavevector  $\mathbf{k}$  has a width that is always *larger* than the peak energy as measured from the Fermi energy; this persists on approach of the Fermi energy, and is opposite to what happens with Landau quasiparticles. The dispersive modes capture the development in the spectral weight of the physical  $f$ -electrons (represented in the model by the  $d$ -operators) in the immediate vicinity of the Fermi energy (SM, Fig. S4A): they appear within a range of the Kondo energy.

What is remarkable is that these dispersive modes form Weyl nodes which are bound near to the Fermi energy, as seen in Fig. 2A (along the high symmetry line,  $-H'-K-H$ , of the Brillouin zone, as marked by the red line that is specified in Figs. 2B,C). They comprise two close-by branches, which are illustrated more clearly in Fig. 2B and Fig. 2C, respectively. To understand the Weyl nodes, we analyze the structure of the interacting Green's function in terms of the Green's function eigenvectors and eigenfunctions. As discussed earlier (and in the SM, Sec. A), the eigenvectors are labeled by the wave vector  $\mathbf{k}$  and are subject to the same crystalline symmetry constraints as Bloch functions. Indeed, the two dispersive modes shown in Fig. 2A have different symmetry eigenvalues and form a symmetry-protected node (see the SM, Sec. H); a

similar mechanism produces additional non-Fermi-liquid Dirac nodes along the high symmetry line  $-A-\Gamma-A$ . In other words, in this model, a robust mechanism underlies the emergence of the Weyl nodes and the associated nodal excitations that go beyond quasiparticles.

We characterize the topological nature of these non-Fermi liquid phases in several ways. We start by analyzing the surface states. Their spectral functions are plotted in Fig. 3A; their exponential decay from the surface to the interior of the system is demonstrated in the SM (Sec. I and Fig. S8A). In addition, in Fig. 3B, we show the in-plane spin-Hall conductivity as a function of  $k_z$  (see the SM, Sec. J), which implicates the topological nature of the Weyl nodes. The overall spin-Hall conductivity has a  $\sqrt{T}$  dependence, as shown in Fig. 3C. At the same time, the nonlinear Hall effect is found to display a singular  $\frac{1}{\sqrt{T}}$  dependence below the Kondo temperature scale (see the SM, Sec. K). We also expect the valley Hall conductivity to have a  $\sqrt{T}$  dependence, as explicitly calculated for a model that shows Dirac nodal states without quasiparticles (see the SM, Fig. S7E). The surface states and the various Hall effects also provide the means to identify the topological semimetal phases experimentally.

Having advanced genuinely interacting Weyl semimetal phases, we now turn to their materials realization. So far we have analyzed the two-channel periodic Anderson model on the 3D kagome lattice, by assuming the existence of the pertinent local degrees of freedom as illustrated in Fig. 1B. From the model studies, we gain the key insight that the form of the electron self-energy is insensitive to the underlying lattice, provided the required local degrees of freedom are in place; for example, its form on the 2D kagome or 3D cubic lattice is essentially the same (see the SM, Fig. S5) as what we have described for the 3D kagome lattice case. We thus look for space group symmetries that constrain nodes in the dispersion while also allowing for the local degrees of freedom of Fig. 1B.

This prescription has led us to three materials, the centrosymmetric PrBi (26) and PrFe<sub>4</sub>P<sub>12</sub> (27) as well as the noncentrosymmetric UPt<sub>3</sub>Au<sub>2</sub> (28), with the space groups #225, #204, and

#216, respectively, and the point group symmetries  $O_h$ ,  $T_h$ , and  $T_d$  at the Pr/U site. The  $\text{Pr}^{3+}$  and  $\text{U}^{4+}$  ions have the electronic configuration  $4f^2$  which, for these point group symmetries, can lead to a  $\Gamma_3$  non-Kramers doublet ground state. A non-Kramers doublet can be treated as pseudo-spin degree of freedom. The first excited levels are then Kramers doublets, whose spin degrees of freedom provide the pseudo-channel index (29). PrBi has a low charge carrier concentration (26),  $\text{PrFe}_4\text{P}_{12}$  can be readily tuned to such a state (27), and  $\text{UPt}_3\text{Au}_2$  (28) exhibits a very weakly temperature-dependent resistivity, all suggestive of semimetallic ground states (see the SM, Sec. L, for further details). Our analysis of space group symmetry constraints suggests the emergence of symmetry protected Dirac nodes in PrBi and  $\text{PrFe}_4\text{P}_{12}$  and symmetry protected Weyl nodes in  $\text{UPt}_3\text{Au}_2$  (see the SM, Sec. M). We have verified our symmetry argument in the representative case of PrBi: Its electronic structure of the non- $f$  conduction electrons (SM, Sec. N) is shown in Fig. S11; symmetry-protected Dirac points away from the Fermi energy are indeed found along the  $\Gamma$ - $X$  line (which also implies that the Kondo-generated emergent excitations in PrBi will have Dirac nodes near the Fermi energy). Thus, to realize the proposed correlated gapless topological phases, we put forward the three as candidate materials for systematic low-temperature studies in their respective phase diagrams.

We close with several important remarks. Firstly, we have already discussed the robustness of our theoretical results for the two-channel Kondo/Anderson lattice models, in that we recover the asymptotically exact low-energy behavior of the self-energy while also uncovering the emergence of a pole in the self-energy. Furthermore, the low-temperature non-Fermi liquid behavior we have presented in the models is consistent with experimental results observed in some (generic-lattice, in particular cubic) heavy-fermion metals that host non-Kramers doublets in the ground-state manifold and, hence, two-channel Kondo lattices (30). Secondly, the loss of quasiparticles in our case is associated with emergent nodal states created by the Kondo effect near the Fermi energy. This is in contrast to the perturbative effect of interactions on

pre-existing nodal states of conduction electrons (3, 4, 31). Thirdly, there can be additional broken-symmetry states at low temperatures, following the paradigm in strongly correlated systems that non-Fermi liquids nucleate novel phases (12). For generic lattices, the multi-channel Kondo correlations may lead to broken-symmetry phases such as superconductivity (32), multipolar order (30) or even time-reversal-symmetry-broken “hastatic” order (33). It will be instructive to explore any new physics that the nontrivial topology brings in these states. Fourthly, the role of electron fractionalization can be further explored in the proposed non-Fermi liquid topological semimetals. The two-channel Kondo effect fractionalizes electrons into Majorana fermions (23), which underlie the loss of Landau quasiparticles. Finally, we have emphasized the constraints of lattice symmetries on dispersive modes associated with peaks of the electron spectral functions. Because it keeps track of both energy and wave vector, our approach will likely allow for constraining the nature of topological states with other types of features in correlations, such as zeros of Green’s functions in topological Mott states (34, 35).

To summarize, our work has advanced the first topological semimetal that has emergent electronic topological excitations beyond quasiparticles and that has no free-electron counterpart. We have advanced a general framework, *viz.* to place symmetry constraints on the dispersive modes of single-particle Green’s functions, which allows us to establish the development of non-Fermi liquid topological semimetals in a robust way. In specific lattices, we have shown how their space group symmetries constrain the two-channel Kondo correlations to produce Weyl (and Dirac) nodal states that are pinned near the Fermi energy but are not quasiparticles. Guided by the considerations of both symmetry and strong correlations, we have proposed several materials to realize these non-Fermi liquid topological semimetals. The proposed approach has the potential to help realize gapless topological phases without free-electron counterparts in a variety of other strongly correlated materials and structures.



## References

1. L. Landau, *Nature* **138**, 840 (1936).
2. D. Xiao, M.-C. Chang, Q. Niu, *Rev. Mod. Phys.* **82**, 1959 (2010).
3. N. P. Armitage, E. J. Mele, A. Vishwanath, *Rev. Mod. Phys.* **90**, 015001 (2018).
4. N. Nagaosa, T. Morimoto, Y. Tokura, *Nature Reviews Materials* **5**, 621 (2020).
5. B. Bradlyn, *et al.*, *Nature* **547**, 298 (2017).
6. J. Cano, *et al.*, *Phys. Rev. B* **97**, 035139 (2018).
7. H. C. Po, A. Vishwanath, H. Watanabe, *Nature Communications* **8**, 50 (2017).
8. H. Watanabe, H. C. Po, M. P. Zaletel, A. Vishwanath, *Phys. Rev. Lett.* **117**, 096404 (2016).
9. B. Bradlyn, *et al.*, *Science* **353** (2016).
10. J. Cano, B. Bradlyn, *Annu. Rev. Condens. Matter Phys.* **12**, 225 (2021).
11. W. Witczak-Krempa, G. Chen, Y. B. Kim, L. Balents, *Annu. Rev. Condens. Matter Phys.* **5**, 57 (2014).
12. S. Paschen, Q. Si, *Nat. Rev. Phys.* **3**, 9 (2021).
13. H.-H. Lai, S. E. Grefe, S. Paschen, Q. Si, *Proceedings of the National Academy of Sciences* **115**, 93 (2018).
14. S. E. Grefe, H.-H. Lai, S. Paschen, Q. Si, *Phys. Rev. B* **101**, 075138 (2020).
15. S. Dzsaber, *et al.*, *Phys. Rev. Lett.* **118**, 246601 (2017).
16. S. Dzsaber, *et al.*, *Proceedings of the National Academy of Sciences* **118** (2021).

17. L. Chen, *et al.*, *arXiv preprint arXiv:2107.10837*; *Nat. Phys.*, in press (2021).
18. H. L. Stormer, D. C. Tsui, A. C. Gossard, *Rev. Mod. Phys.* **71**, S298 (1999).
19. A. A. Abrikosov, L. P. Gorkov, I. E. Dzyaloshinski, *Methods of quantum field theory in statistical physics* (Courier Corporation, 2012).
20. S. Kirchner, *Advanced Quantum Technologies* **3**, 1900128 (2020).
21. I. Affleck, A. W. W. Ludwig, *Phys. Rev. B* **48**, 7297 (1993).
22. V. J. Emery, S. Kivelson, *Phys. Rev. B* **46**, 10812 (1992).
23. J. M. Maldacena, A. W. Ludwig, *Nuclear Physics B* **506**, 565 (1997).
24. G. Kotliar, D. Vollhardt, *Physics today* **57**, 53 (2004).
25. D. L. Cox, A. E. Ruckenstein, *Phys. Rev. Lett.* **71**, 1613 (1993).
26. X. He, *et al.*, *Phys. Rev. B* **101**, 075106 (2020).
27. H. Hidaka, *et al.*, *Phys. Rev. B* **71**, 073102 (2005).
28. C. Quitmann, *et al.*, *Phys. Rev. B* **38**, 6432 (1988).
29. D. L. Cox, A. Zawadowski, *Advances in Physics* **47**, 599 (1998).
30. A. Sakai, S. Nakatsuji, *J. Phys. Soc. Japan* **80**, 063701 (2011).
31. E.-G. Moon, C. Xu, Y. B. Kim, L. Balents, *Phys. Rev. Lett.* **111**, 206401 (2013).
32. M. Tsujimoto, Y. Matsumoto, T. Tomita, A. Sakai, S. Nakatsuji, *Phys. Rev. Lett.* **113**, 267001 (2014).
33. P. Chandra, P. Coleman, R. Flint, *Nature* **493**, 621 (2013).

34. T. Morimoto, N. Nagaosa, *Sci. Rep.* **6**, 19853 (2016).
35. P. Mai, B. Feldman, P. W. Phillips, *arXiv preprint arXiv:2207.01638* (2022).
36. V. Gurarie, *Phys. Rev. B* **83**, 085426 (2011).
37. Z. Wang, X.-L. Qi, S.-C. Zhang, *Phys. Rev. B* **85**, 165126 (2012).
38. P. Nozieres, A. Blandin, *Journal de Physique* **41**, 193 (1980).
39. M. Pustilnik, L. Borda, L. I. Glazman, J. von Delft, *Phys. Rev. B* **69**, 115316 (2004).
40. A. J. Keller, *et al.*, *Nature* **526**, 237 (2015).
41. Z. Iftikhar, *et al.*, *Nature* **526**, 233 (2015).
42. S.-S. Yeh, *et al.*, *Nature Communications* **11**, 4749 (2020).
43. A. Cai, Z. Yu, H. Hu, S. Kirchner, Q. Si, *Phys. Rev. Lett.* **124**, 027205 (2020).
44. A. Georges, G. Kotliar, Q. Si, *International Journal of Modern Physics B* **06**, 705 (1992).
45. J. Kroha, P. Wölfle, *Advances in Solid State Physics 39* (Springer Berlin Heidelberg, Berlin, Heidelberg, 1999), pp. 271–280.
46. M. H. Hettler, J. Kroha, S. Hershfield, *Phys. Rev. B* **58**, 5649 (1998).
47. F. B. Anders, *Phys. Rev. B* **71**, 121101 (2005).
48. M. Jarrell, H. Pang, D. L. Cox, K. H. Luk, *Phys. Rev. Lett.* **77**, 1612 (1996).
49. Y. Michishita, R. Peters, *Phys. Rev. B* **103**, 195133 (2021).
50. Z. Z. Du, C. M. Wang, H.-P. Sun, H.-Z. Lu, X. C. Xie, *Nature Communications* **12**, 5038 (2021).

51. A. Vashist, R. K. Gopal, D. Srivastava, M. Karppinen, Y. Singh, *Phys. Rev. B* **99**, 245131 (2019).
52. Z. Wu, *et al.*, *Phys. Rev. B* **99**, 035158 (2019).
53. S. H. Curnoe, H. Harima, K. Takegahara, K. Ueda, *Phys. Rev. B* **70**, 245112 (2004).
54. H. Sugawara, *et al.*, *Phys. Rev. B* **66**, 134411 (2002).
55. G. Kresse, J. Hafner, *Phys. Rev. B* **48**, 13115 (1993).
56. G. Kresse, J. Furthmüller, *Computational Materials Science* **6**, 15 (1996).
57. A. D. Becke, E. R. Johnson, *The Journal of chemical physics* **124**, 221101 (2006).
58. F. Tran, P. Blaha, *Phys. Rev. Lett.* **102**, 226401 (2009).
59. G. Kresse, D. Joubert, *Phys. Rev. B* **59**, 1758 (1999).
60. D. Hobbs, G. Kresse, J. Hafner, *Phys. Rev. B* **62**, 11556 (2000).

**Acknowledgments:** Work at Rice has been supported by the the National Science Foundation under Grant No. DMR-2220603 (L.C. and Q.S.), the Air Force Office of Scientific Research under Grant No. FA9550-21-1-0356 (C.S.) and the Robert A. Welch Foundation Grant No. C-1411 (H.H.). The majority of the computational calculations have been performed on the Shared University Grid at Rice funded by NSF under Grant EIA-0216467, a partnership between Rice University, Sun Microsystems, and Sigma Solutions, Inc., the Big-Data Private-Cloud Research Cyberinfrastructure MRI-award funded by NSF under Grant No. CNS-1338099, and the Extreme Science and Engineering Discovery Environment (XSEDE) by NSF under Grant No. DMR170109. M.G.-D. and M.G.V. acknowledge support from the Spanish Ministry of Science and Innovation Grant No. PID2019-109905GB-C21 and the Deutsche Forschungsgemeinschaft (DFG, German Research Foundation) GA 3314/1-1 – FOR 5249 (QUAST). Work

at Los Alamos was carried out under the auspices of the U.S. Department of Energy (DOE) National Nuclear Security Administration under Contract No. 89233218CNA000001, and was supported by LANL LDRD Program. A.P. and S.P. acknowledge funding from the Austrian Science Fund (projects No. I4047 and 29279), the European Microkelvin Platform (H2020 project No. 824109) and the FWF via the Research unit QUASt-FOR5249. S.K. was in part supported by the Ministry of Science and Technology, Taiwan (grant No. MOST 111-2634-F-A49-007) and the Center for Emergent Functional Matter Science of National Yang Ming Chiao Tung University from “The Featured Areas Research Center Program” within the framework of the “Higher Education Sprout Project by the Ministry of Education (MOE)” in Taiwan, by the Yusha Fellowship Program of the MOE Taiwan, and by the National Key R&D Program of the MOST of China, Grant No. 2016YFA0300202 and the National Science Foundation of China, Grant No. 11774307. J.C. acknowledges the support of the National Science Foundation under Grant No. DMR-1942447 and the support of the Flatiron Institute, a division of the Simons Foundation. Four of us (S.G., S.P., J.C. and Q.S.) acknowledge the hospitality of the Aspen Center for Physics, which is supported by NSF grant No. PHY-1607611.

**Authors contributions:** All authors contributed to the research of the work and the writing of the paper.

**Competing interests:** The authors have no competing interests.

**Data availability:** The data that support the findings of this study are available from the corresponding author upon reasonable request.

\*To whom correspondence should be addressed; E-mail: qmsi@rice.edu.

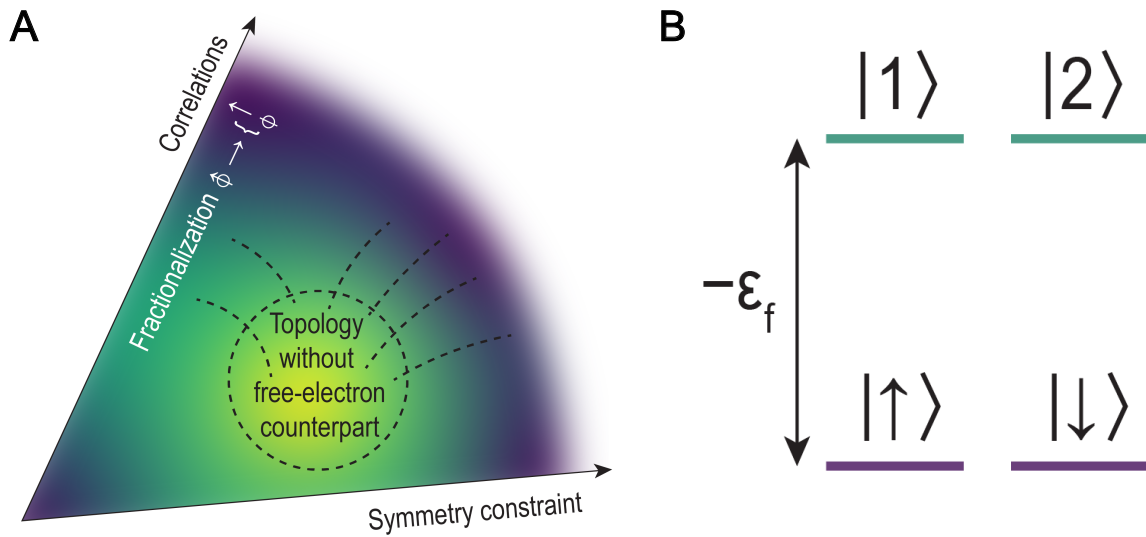


Figure 1: **Illustration of the proposed route for electronic topological phases without quasi-particles.** (A) An approach for topological phases without free-electron counterparts: Lattice symmetries constrain emergent excitations that are induced by strong correlations and particularly fractionalization. (B) Strongly correlated local degrees of freedom involved in the two-channel Anderson lattice model.

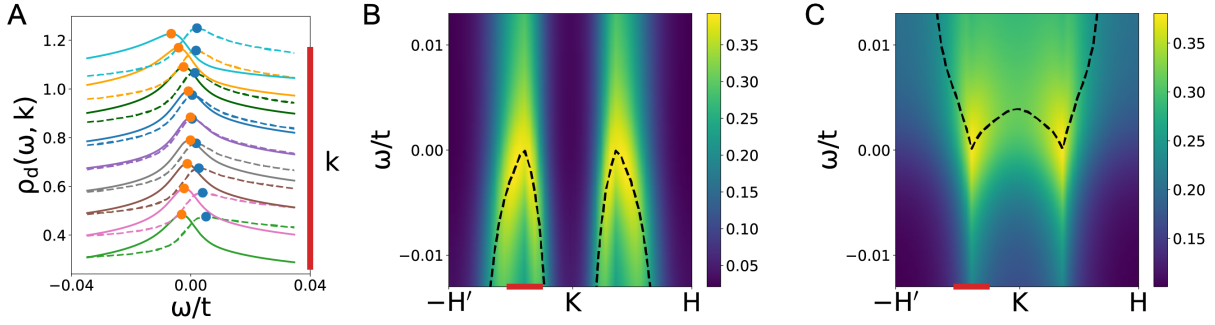


Figure 2: **Emergence of Weyl nodal excitations beyond quasiparticles.** (A) The  $d$  electron spectral functions ( $\rho_d$ ) at various  $k$  points (marked by the red bar on the right) along a high symmetry line in the 3D kagome lattice. Solid and dashed lines denote two dispersive modes from two eigenvalues of the Green's function. The blue and orange dots label the positions of the spectral peaks, which meet at a Weyl point. Each  $\rho_d$  curve has been shifted vertically to avoid overlapping. (B),(C) illustrate the spectral functions of the two Weyl-point-bearing branches. Here, the dashed line denotes the energy spectral peaks. The red bar marks the cut of wave vectors in the Brillouin zone along which the spectral functions are shown in panel A. The calculations are done at the temperature  $T = 10^{-3}T_K$ .

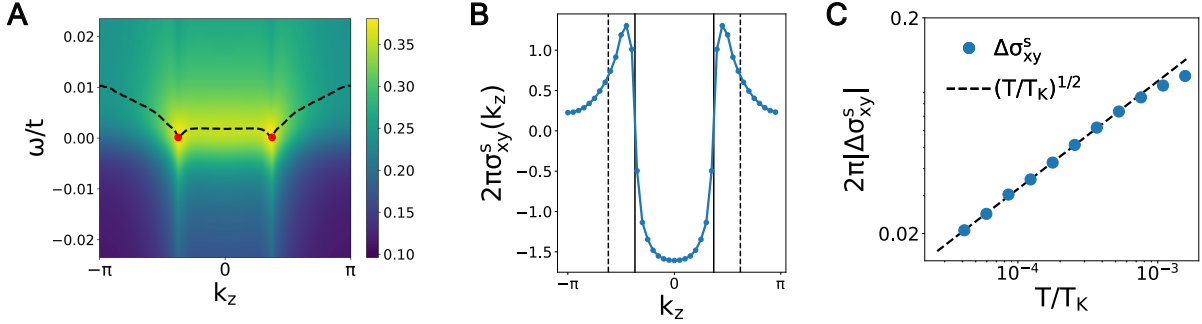


Figure 3: **Characterizing the topological nature of the correlated phase.** (A) The spectrum of the edge mode at  $k_x = 4\pi/3$  in the 3D kagome lattice at  $T/T_K = 10^{-3}$  with an open boundary along the  $y$  direction; the two red dots mark the Weyl nodes; the dashed line denotes the energy spectral peak. (B) In-plane spin-Hall conductivity  $\sigma_{xy}^s$  as a function of  $k_z$  in the 3D kagome model at  $T/T_K = 10^{-3}$ . The vertical solid/dashed lines mark the  $k_z$  coordinates of the planes in which the Weyl/Dirac nodes reside. A rapid change (in the form of a smeared jump) occurs when  $k_z$  crosses the Weyl/Dirac-node-hosting planes. (C) The total spin Hall conductivity of the 3D kagome model showing a  $\sqrt{T}$  dependence. Here, the extrapolated zero-temperature value ( $\sim 0.25$ ) is subtracted in order to highlight the nature of the  $T$ -dependent component.



# Supplementary Materials

## Topological semimetals without quasiparticles

Haoyu Hu, Lei Chen, Chandan Setty, Mikel Garcia-Diez, Sarah E. Grefe, Andrey Prokofiev, Stefan Kirchner, Maia G. Vergniory, Silke Paschen, Jennifer Cano, and Qimiao Si\*

\*To whom correspondence should be addressed; E-mail: qmsi@rice.edu.

Materials and Methods

Figs. S1–S11

References (36–60, see above)

## Materials and Methods

### A. Symmetry of Green’s function: Space group symmetry constraints on interacting systems

We study the symmetry properties of the Green’s functions:

$$[G(\tau, \mathbf{r}, \tau', \mathbf{r}')]_{ab} = -\langle T_\tau \psi_{a,\mathbf{r},\tau} \psi_{b,\mathbf{r},\tau'}^\dagger \rangle,$$

where  $\psi_{a,\mathbf{r},\tau}^\dagger$  creates an electron with index  $a$ , which characterizes its spin, orbital and sublattice, at position  $\mathbf{r}$  and imaginary time  $\tau$ . We will first prove that, in a quantum phase with symmetry of the space group  $H$ , the eigenvectors of the Green’s function form a representation of both  $H$  and the corresponding little group  $H_{\mathbf{k}}$ . Based on these symmetry properties, we can analyze the symmetry-protected crossing of single-particle excitations.

In general, it is more convenient to work with Matsubara frequency and wave vector by

introducing Fourier transformation of electron operators:

$$\psi_{a,i\omega,\mathbf{k}} = \frac{1}{\beta N} \sum_{\mathbf{r}} \int_0^\beta \psi_{a,\mathbf{r},\tau} e^{i\omega\tau - i\mathbf{k}\cdot\mathbf{r}} d\tau,$$

where  $N$  is the total number of unit cells and  $\beta$  is the inverse temperature. The Fourier transformation leads to following Green's function,  $[G]_{(a,i\omega,\mathbf{k}),(b,i\omega',\mathbf{k}')} = -\langle \psi_{a,i\omega,\mathbf{k}} \psi_{b,i\omega',\mathbf{k}'}^\dagger \rangle$ , which can be treated as a matrix with row index  $(a, i\omega, \mathbf{k})$  and column index  $(b, i\omega', \mathbf{k}')$ . As a matrix, we can introduce the eigenvectors and eigenvalues:

$$\frac{1}{N\beta} \sum_{b,i\omega',\mathbf{k}'} [G]_{(a,i\omega,\mathbf{k}),(b,i\omega',\mathbf{k}')} [v_i]_{(b,i\omega',\mathbf{k}')} = g_i [v_i]_{(a,i\omega,\mathbf{k})},$$

where  $g_i$  and  $[v_i]_{(a,i\omega,\mathbf{k})}$  denote the  $i$ -th eigenvalue and  $i$ -th eigenvector.

We then prove the set of all eigenvectors  $\{v_i\}_{i=1,2,\dots}$  form a representation space of the space group  $H$  whose element is defined as

$$h \in H : \psi_{a,i\omega,\mathbf{k}} \rightarrow \sum_b [U_h^\dagger(\mathbf{k})]_{ab} \psi_{b,i\omega,h\mathbf{k}},$$

where  $U_h(\mathbf{k})$  is a unitary matrix. The symmetry of the system requires the Green's function to satisfy

$$[\mathcal{U}_h^\dagger G \mathcal{U}_h]_{(a,i\omega,\mathbf{k}),(b,i\omega',\mathbf{k}')} = [G]_{(a,i\omega,\mathbf{k}),(b,i\omega',\mathbf{k}')} ,$$

where  $[\mathcal{U}_h]_{(a,i\omega,\mathbf{k}),(b,i\omega',\mathbf{k}')} = \delta_{\omega,\omega'} \delta_{\mathbf{k}',h\mathbf{k}} U_h(\mathbf{k})$ . Consequently,  $[\mathcal{U}_h v_i]_{(a,i\omega,\mathbf{k})}$  is also an eigenvector of the Green's function matrix  $[G]$  and we can then introduce the matrix representation  $\mathcal{D}[h]$  of  $h \in H$  via

$$[\mathcal{U}_h v_i]_{a,i\omega,\mathbf{k}} = \sum_j \mathcal{D}[h]_{ij} [v_j]_{a,i\omega,\mathbf{k}} .$$

Therefore, the set of all eigenvectors  $\{v_i\}_{i=1,2,\dots}$  form a representation of space group  $H$  with matrix representation  $\mathcal{D}[h]$ .

In practice, the systems we deal with hold space and time translation symmetry, which allows us to decompose  $G$  into block diagonal forms

$$[G]_{(a,i\omega,\mathbf{k}),(b,i\omega',\mathbf{k}')} = \delta_{\omega,\omega'}\delta_{\mathbf{k},\mathbf{k}'}[G(i\omega,\mathbf{k})]_{ab}.$$

We also perform an analytical continuation by replacing  $i\omega$  with  $\omega + i0^+$  and work with the retarded Green's function. Due to the block diagonalized structure, it's enough to consider the eigenvalues and eigenvectors of each block characterized by  $(\omega, \mathbf{k})$  (19, 36, 37):

$$\sum_b [G(\omega, \mathbf{k})]_{ab} [v_i(\omega, \mathbf{k})]_b = g_i(\omega, \mathbf{k}) [v_i(\omega, \mathbf{k})]_a,$$

where  $g_i(\omega, \mathbf{k})$  and  $[v_i(\omega, \mathbf{k})]_b$  are the  $i$ -th eigenvalue and  $i$ -th eigenvector of each block. We define the  $i$ -th mode in terms of the combination of  $g_i(\omega, \mathbf{k})$  and  $v_i(\omega, \mathbf{k})$ . The corresponding spectral function of the  $i$ -th mode is

$$\rho_i(\omega, \mathbf{k}) = -\frac{1}{\pi} \text{Im}[g_i(\omega, \mathbf{k})].$$

The full spectral function is then the sum of spectral functions of each mode

$$\rho(\omega, \mathbf{k}) = -\frac{1}{\pi} \text{TrIm}[G(\omega, \mathbf{k})] = \sum_i \rho_i(\omega, \mathbf{k}).$$

To analyze the symmetry properties of the dispersive modes, it's useful to consider the little group  $H_{\mathbf{k}} \leq H$ . For a given  $\mathbf{k}$  in the first Brillouin zone, the little group  $H_{\mathbf{k}}$  is defined as  $H_{\mathbf{k}} = \{h \in H | h\mathbf{k} = \mathbf{k}\}$  (10). Since the symmetry operation  $h \in H_{\mathbf{k}}$  won't change the wave vector  $\mathbf{k}$ , we can focus on the set of eigenvectors  $\{v_i(\omega, \mathbf{k})\}_{i=1,2,\dots}$  with the wave vector index  $\mathbf{k}$ . As we mentioned earlier, the eigenvectors form a representation space of the space group  $H$ . Thus, the eigenvectors of the  $\mathbf{k}$  block,  $\{v_i(\omega, \mathbf{k})\}_{i=1,2,\dots}$ , form a representation space of the little group  $H_{\mathbf{k}}$ , which is also a subgroup of  $H$ . The matrix representation  $D_{\omega,\mathbf{k}}[h]$  for  $h \in H_{\mathbf{k}}$  is defined via

$$[U_h(\mathbf{k})v_i(\omega, \mathbf{k})]_a = \sum_j \left[ D_{\omega,\mathbf{k}}[h] \right]_{ij} [v_j(\omega, \mathbf{k})]_a. \quad (\text{S1})$$

We can further decompose the representation into a direct sum of irreducible representations and analyze their symmetry properties. In this way, the lattice symmetry operates in interacting systems on the eigenfunctions of the Green's function in parallel to how it acts in noninteracting systems on the Bloch functions (5–10).

Based on the representation decomposition, we can inspect the dispersive modes of each irreducible representation. As we continuously tune  $k$ , if the peaks of two dispersive modes from two different irreducible representations cross, then such crossing cannot be gapped out by symmetry preserved perturbations. Another type of symmetry-protected crossing could appear when we tune the  $k$  to certain high symmetry points, where additional symmetry leads to a two or higher dimensional irreducible representation. In this case, the spectral functions of the corresponding dispersive modes must degenerate. A detailed explanation of the symmetry-protected Weyl/Dirac node in our microscopic model is provided in this SM (Sec. H).

## **B. Periodic Anderson model with two channels of conduction electrons**

We consider a two-channel periodic Anderson model. While such a model can be considered in a generic setting for correlation physics, we focus on two representative lattices in which crystalline symmetries promote Dirac and Weyl nodes. At every site, the local degrees of freedom (Fig. 1B) hybridize with two channels of conduction electrons, labeled by  $\alpha = 1, 2$ ; the hybridization involves the change of local electron number by 1, which turns the local configuration to  $|\alpha = 1, 2\rangle$ , and likewise from  $|\alpha\rangle$  to  $|\sigma\rangle$ . In practice, one way of realizing the two-channel periodic Kondo/Anderson model is to use an orbital degree of freedom (non-Kramers doublet such as  $\Gamma_3$ ) to represent the pseudo-spin  $\sigma$  leaving the physical spins of the conduction electrons and a higher Kramers doublet to represent the channel  $\alpha$  (29, 30). The single-impurity version of this model, the two-channel Anderson/Kondo model, is well established to have non-Fermi liquid behavior (20, 21, 29, 38–42); the electron correlations fractionalize the  $d$ -electron,

leading to an emergent Majorana fermion (22, 23).

We consider both 3D and 2D kagome lattices, where the 3D kagome lattice corresponds to the stacking of the kagome planes with two added ingredients – the inversion symmetry is broken and a non-zero spin orbit coupling reduces the  $SU(2)$  spin symmetry down to the  $U(1)$  spin symmetry (see Sec. C). The model can be expressed in terms of the following Hamiltonian:

$$\begin{aligned} \mathcal{H} = & \sum_{ij,\sigma,\alpha} (t_{ij,\sigma\sigma'} - \mu\delta_{ij}\delta_{\sigma\sigma'}) c_{i,\sigma,\alpha}^\dagger c_{j,\sigma',\alpha} \\ & + P \left[ \epsilon_f \sum_{i,\sigma,\alpha} d_{i,\sigma,\alpha}^\dagger d_{i,\sigma,\alpha} + V \sum_{i,\sigma,\alpha} (c_{i,\sigma,\alpha}^\dagger d_{i,\sigma,\alpha} + \text{h.c.}) \right] P. \end{aligned} \quad (\text{S2})$$

Here,  $c_{i,\sigma,\alpha}$  ( $d_{i,\sigma,\alpha}$ ) denotes a conduction (local) electron of spin  $\sigma$  and channel  $\alpha$  on site  $i$ , which marks both the unit cell position and sub-lattice index. The projection operator  $P$  allows for the strongly correlated  $d$ -electrons to have two empty states  $|1\rangle, |2\rangle$  and two singly occupied states  $|\uparrow\rangle, |\downarrow\rangle$  at every site. In addition,  $t_{ij,\sigma\sigma'}$  is the hopping matrix of the conduction electrons, with  $\mu$  acting as the chemical potential;  $\epsilon_f$  specifies the spacing of the  $d$ -electron levels (Fig. 1B), and  $V$  is the hybridization strength between the two types of electrons. We solve the model within dynamical mean-field theory (DMFT) (24) as described in this SM, Sec. D; importantly, we utilize a dynamical large- $N$  method that captures the asymptotic low-energy behavior of the two-channel Kondo model (25, 43) (see Sec. D).

### C. Noninteracting band structure

The noninteracting Hamiltonian of the 3D kagome lattice is

$$\begin{aligned} \mathcal{H}_0 = & \sum \begin{bmatrix} c_{\mathbf{k},\alpha,\uparrow}^\dagger & c_{\mathbf{k},\alpha,\downarrow}^\dagger \end{bmatrix} \begin{bmatrix} h(\mathbf{k}) - \mu\mathbb{I} & \\ & h^*(-\mathbf{k}) - \mu\mathbb{I} \end{bmatrix} \begin{bmatrix} c_{\mathbf{k},\alpha,\uparrow} \\ c_{\mathbf{k},\alpha,\downarrow} \end{bmatrix} \\ c_{\mathbf{k},\alpha,\sigma} = & \begin{bmatrix} c_{A,\mathbf{k},\alpha,\sigma} & c_{B,\mathbf{k},\alpha,\sigma} & c_{C,\mathbf{k},\alpha,\sigma} \end{bmatrix}^T. \end{aligned} \quad (\text{S3})$$

Here,  $A, B, C$  denote three sublattices located at  $(\frac{1}{4}, \frac{\sqrt{3}}{4}, 0)a, (\frac{1}{2}, 0, 0)a, (\frac{1}{4}, -\frac{\sqrt{3}}{4}, 0)a$  respectively (thus, each unit cell has three sites). The hopping matrix in the spin up sector is:

$$\begin{aligned}
h(k) = & [t - t_{z,2} \cos(k_z)] \\
& \begin{bmatrix} 0 & [(1+\alpha) + (1-\alpha)e^{-ik_2}] & [(1+\alpha)e^{ik_1} + (1-\alpha)e^{-ik_2}] \\ [(1+\alpha) + (1-\alpha)e^{ik_2}] & 0 & [(1+\alpha)e^{ik_1} + (1-\alpha)] \\ [(1+\alpha)e^{-ik_1} + (1-\alpha)e^{ik_2}] & [(1+\alpha)e^{-ik_1} + (1-\alpha)] & 0 \end{bmatrix} \\
& -t_z \cos(k_z) \begin{bmatrix} 1 & 0 & 0 \\ 0 & 1 & 0 \\ 0 & 0 & 1 \end{bmatrix} - t_2 \begin{bmatrix} 0 & [e^{i(-k_1-k_2)} + e^{ik_1}] & (1 + e^{i(k_1-k_2)}) \\ [e^{i(k_1+k_2)} + e^{-ik_1}] & 0 & [e^{i(k_1+k_2)} + e^{-ik_2}] \\ [1 + e^{-i(k_1-k_2)}] & [e^{-i(k_1+k_2)} + e^{ik_2}] & 0 \end{bmatrix} \\
& + [i\lambda + i\lambda_z \cos(k_z)] \begin{bmatrix} 0 & [1 + e^{-ik_2}] & [-e^{ik_1} - e^{-ik_2}] \\ -[1 + e^{ik_2}] & 0 & [1 + e^{ik_1}] \\ [e^{-ik_1} + e^{ik_2}] & -[1 + e^{-ik_1}] & 0 \end{bmatrix},
\end{aligned}$$

where

$$k_{1/2} = \frac{1}{2}(k_x \pm \frac{k_y}{\sqrt{3}}).$$

In addition,  $t, t_2$  are the nearest-neighbor and next-nearest-neighbor intra-layer hopping parameters, and  $t_z$  and  $t_{z,2}$  are the nearest-neighbor and next-nearest-neighbor inter-layer hopping elements.  $\alpha$  denotes the anisotropy of  $t_1$  and  $t_{z,2}$  hopping that breaks mirror symmetry  $M_y$  and inversion symmetry.  $\lambda$  and  $\lambda_z$  are the intra-layer and inter-layer spin orbit couplings, respectively, which reduce the  $SU(2)$  spin symmetry down to  $U(1)$ . The corresponding 2D kagome model without spin-orbit coupling and inversion symmetry breaking can be realized by setting  $t_z = t_{z,2} = \lambda = \lambda_z = 0, \alpha = 0$  and dropping all the terms that contain  $k_z$ .

In practice, we set  $t_1 = 0.29, t_2 = 0.14, t_z = -0.17, t_{z,2} = 0.26, \lambda = 0.43, \lambda_z = 0.06, \alpha = 1.4, \mu = -1.09$  for the 3D kagome lattice. As shown in Fig. S1B, Fig. S1E and Fig. S1F, we observe two Weyl nodes at  $(1/3, 1/3, z), (2/3, 2/3, -z)$ , two anti-Weyl nodes at  $(1/3, 1/3, -z), (2/3, 2/3, z)$ , and two Dirac nodes at  $(0, 0, \pm z')$  where  $z \approx 0.19, z' \approx 0.32$ . Weyl and Dirac nodes are all protected by  $C_{3z}$  symmetry. In Fig. S1E and Fig. S1F, we label the relevant bands by their eigenvalues of  $C_{3z}$  symmetry, where  $\eta = e^{i2\pi/6}$ . The  $C_{3z}$  symmetry excludes the

hybridization between the two bands with different eigenvalues, and thus protects the nodes. The bands along the high symmetry line ( $-A-\Gamma-A$ ) are two-fold degenerate due to the mirror symmetry  $M_z$  and time-reversal symmetry. The eigenvalues inside (outside) the brackets are for the spin-up (spin-down) sector. Because the hybridization between spin-up and spin-down electrons is forbidden by the  $U(1)$  spin symmetry, there can be no gap opened by hybridizing two bands with the same  $C_{3z}$  eigenvalue but opposite spin indices.

For the 2D kagome lattice, we set  $t_1 = 1, t_2 = 0.3, \mu = -1.0$ . (We have chosen generic parameters so that the band structure is relatively simple.) The noninteracting dispersion and Dirac node are shown in Fig. S1D. At the high symmetry point  $K/K'$ , three bands form  $\Gamma_1 \oplus \Gamma_3$  representations of the little group  $C_{3v}$ , where  $\Gamma_3$  is a two-dimensional irreducible representation and thus protects the Dirac node. Here, due to the  $SU(2)$  symmetry, we consider the spinless representations of the group.

## D. Solution methods: Dynamical mean-field theory and the dynamical large- $N$ approach

The two-channel Kondo effect is a robust mechanism for non-Fermi liquid physics (21). Here, we describe the dynamical method that captures the asymptotic low-energy form of the non-Fermi liquid behavior (25, 43), while incorporating the lattice symmetries that can constrain the emergent electronic excitations.

To solve the lattice model, we first introduce the auxiliary-particle representation of the projected local electron annihilation operator:  $Pd_{i,\sigma,\alpha}P = f_{i,\sigma}b_{i,\alpha}^\dagger$ . Here,  $f_{i,\sigma}$  is a pseudo-fermion annihilation operator and  $b_{i,\alpha}^\dagger$  is a pseudo-boson creation operator. The Hilbert space of the  $d$  electron can be expressed as:  $|\sigma\rangle = f_\sigma^\dagger|\text{vac}\rangle, |\alpha\rangle = b_\alpha^\dagger|\text{vac}\rangle$  with the vacuum state  $|\text{vac}\rangle$ . There is also a local constraint on the pseudo-particle occupation numbers,  $Q_i = \sum_\sigma f_{i,\sigma}^\dagger f_{i,\sigma} + \sum_\alpha b_{i,\alpha}^\dagger b_{i,\alpha} = 1$ .

In DMFT, the local correlators of the two-channel periodic Anderson model is determined by the self-consistent local model (44):

$$\begin{aligned}
S_{loc} &= \int \sum_{\sigma,\alpha} c_{\sigma,\alpha}^\dagger(\tau) G_0(\tau, \tau')^{-1} c_{\sigma,\alpha}(\tau') d\tau d\tau' \\
&+ \int \left[ \sum_{\sigma} f_{\sigma}^\dagger(\tau) (\partial_{\tau} - \epsilon_f) f_{\sigma}(\tau) + \sum_{\alpha} b_{\alpha}^\dagger(\tau) \partial_{\tau} b_{\alpha}(\tau) \right] d\tau \\
&+ \int V \sum_{\sigma,\alpha} (c_{\alpha,\sigma}^\dagger(\tau) f_{\sigma}(\tau) b_{\alpha}^\dagger(\tau) + h.c.) d\tau \\
&+ \int i\lambda(\tau) \left( \sum_{\sigma} f_{\sigma}^\dagger(\tau) f_{\sigma}(\tau) + \sum_{\alpha} b_{\alpha}^\dagger(\tau) b_{\alpha}(\tau) - Q \right) d\tau. \tag{S4}
\end{aligned}$$

Here,  $\lambda$  is a Lagrangian multiplier enforcing the pseudo-particle constraint. Whereas  $G_0$  is the bath function of the conduction electrons, which is determined from the DMFT equations:

$$\begin{aligned}
G_{c,loc}(\omega) &= \frac{1}{L^d} \sum_{\mathbf{k}} \frac{1}{\omega - t_{\mathbf{k}} - \Sigma_c(\omega)} \\
G_0^{-1}(\omega) - G_{c,loc}^{-1}(\omega) &= \Sigma_c(\omega). \tag{S5}
\end{aligned}$$

$G_{c,loc}(\omega)$  is the local Green's function of the  $c$  electrons,  $\Sigma_c(\omega)$  is the associated self-energy which is taken to be local, i.e.,  $\mathbf{k}$ -independent within the DMFT. We note that the effective local model in the 3D lattice model has an effective  $SU(2)$  spin symmetry. The bath functions for the spin up and spin down conduction electrons are the same due to the time reversal symmetry and no hybridization between spin up and spin down electrons is allowed given the  $U(1)$  spin symmetry.

The local model is solved via the saddle point equations (25, 45–47) of a dynamical large- $N$  limit [with a generalization to an  $SU(N)$  symmetry for the local electrons' spins and an  $SU(N) \times SU(M)$  symmetry for the conduction electrons, while taking the large- $N, M$  limit



with a fixed  $N/M = 1$ ]. Here, the self-energies of the pseudo-fermion and pseudo-boson are

$$\begin{aligned}\Sigma_f(\omega) &= MV^2 \int \rho_0(\omega - \epsilon) f(\epsilon - \omega) G_b(\epsilon) d\epsilon \\ \Sigma_b(\omega) &= NV^2 \int \rho_0(\epsilon - \omega) f(\epsilon - \omega) G_f(\epsilon) d\epsilon\end{aligned}$$

where  $\rho_0$  is the density of states associated with the bath function  $G_0$  and  $f(x)$  is the Fermi-Dirac function. In conjunction with the Dyson equations for the pseudo-particle propagators  $G_f, G_b$ ,

$$\begin{aligned}G_f^{-1}(\omega) &= \omega - \epsilon_f - \lambda - \Sigma_f(\omega) \\ G_b^{-1}(\omega) &= \omega - \lambda - \Sigma_b(\omega),\end{aligned}$$

we have a complete set of equations. The local Green's function is calculated via  $G_{c,loc}(\omega) = G_0(\omega) + V^2 G_0(\omega) G_d(\omega) G_0(\omega)$ , with  $G_d(\omega)$  being the correlator of the  $d$  electron. We note that  $V$  is at the order of  $1/\sqrt{N}$  in the large- $N$  approach. These equations are known to capture the asymptotic low-energy behavior – including the non-Fermi liquid exponents - of the multi-channel Kondo/Anderson models (25). Importantly, the  $1/N$  vertex corrections do not change the asymptotic low-energy behavior (25, 43).

In practice, we take  $V = 1.0, \epsilon_f = -0.5$  for the 2D kagome model and  $V = 1.5, \epsilon_f = -1.0$  for the 3D kagome model. We work on the retarded Green's functions and solve the DMFT self-consistent equation by varying the bath function  $G_{c,0}$  and stop the procedure when the difference between two iterations is less than 1%.

We solve the dynamical large- $N$  equations in real frequency. It turns out to be important to reach sufficiently low temperatures (down to about  $10^{-3} - 10^{-5}$  of the Kondo temperature  $T_K$ ) in order to reveal the asymptotic low-energy behavior. We find  $T_K/t \approx 0.03$  for the model on the 3D kagome lattice and  $T_K/t \approx 0.01$  for the model on the 2D kagome lattice.

In Fig. S3A and Fig. S3B, we show the local spectral functions of the pseudo-bosons and

pseudo-fermions of the 3D kagome lattice. We observe an  $\omega/T$  scaling with

$$\begin{aligned}\rho_f(\omega, T) &= \left(\frac{T}{T_K}\right)^{1/2} g_f(\omega/T) \\ \rho_b(\omega, T) &= \left(\frac{T}{T_K}\right)^{1/2} g_b(\omega/T),\end{aligned}\tag{S6}$$

where  $g_f(x), g_b(x)$  are universal functions. The results for the 2D kagome lattice (not shown) are very similar. In addition, to illustrate the power-law dependence, Fig. S3C and Fig. S3D depict  $\rho_b$  vs. frequency at a low temperature for the 3D and 2D kagome lattices, respectively.

## E. Breakdown of quasiparticles

The imaginary part of the conduction-electron self-energy,  $\text{Im}\Sigma_c(\omega)$ , is found to depend on frequency in a square-root fashion in the low-energy limit, as shown in Fig. S2A. This is in contrast to the Fermi liquid case, where  $\text{Im}\Sigma_c(\omega)$  goes quadratically in  $\omega$ . The square-root frequency dependence of the self-energy describes a non-Fermi liquid, with a loss of quasiparticles. The non-Fermi liquid behavior is characterized by an electrical resistivity that depends on temperature ( $T$ ) in a  $\sqrt{T}$  way, which is illustrated in Fig. S2B. In practice, we find that the asymptotic behavior, in both the frequency and temperature dependences, appears only at sufficiently low temperatures; it was not found in previous DMFT solutions of the multichannel Kondo lattice model on the infinite dimensional hypercubic lattice (48) solved at much higher temperatures (about  $0.1 T_K$  and above).

The self-energy can be described by a form that contains both the asymptotic low-energy behavior and a pole in the complex energy plane.

$$\Sigma_c(\omega) \sim A \frac{\gamma}{\omega - \omega_0 + i\gamma} + g(\omega) \Theta(\Lambda - |\omega|),\tag{S7}$$

where  $\Theta(x)$  is the Heaviside step function, and  $g(\omega) \sim a + c\sqrt{|\omega|}$  describes the low-energy asymptotic behavior that appears below the energy cutoff  $\Lambda$ . (For further details, see Sec. F.) To

our knowledge, the existence of a pole in the self-energy has not been recognized in any two-channel Kondo model; its uncovering is made possible by our working on the real-frequency axis and solving the model at very low temperatures. Physically, the pole captures the development of the  $f$ -electron spectral weight within an energy range of  $T_K$  near the Fermi energy. Because the  $f$ -electron state can decay into the fractionalized (Majorana) excitations, the damping rate  $\gamma$  remains nonzero even at the zero-temperature limit.

The structure of the self-energy implies two branches of dispersive modes near the Fermi energy  $E_F$ , with velocities highly reduced by the factor  $\sim T_K/D$ , where  $D$  is the bare bandwidth (see Sec. F).

## **F. Self-energy: asymptotic low energy behavior, a pole and the resulting emergent dispersive modes**

In this section, we describe the nature of the self-energy  $\Sigma_c$  in some detail. Due to the symmetry requirement, the local self-energy  $\Sigma_c$  is diagonal in spin, sublattice and channel spaces, which simplifies the analysis. As shown in Fig. S4A,  $\text{Im}[\Sigma_c](\omega)$  has a peak near the Fermi energy. We find that this peak is well represented by a Lorentzian function; we define the peak center and width as  $\omega_0$  and  $\gamma$ , respectively. Accordingly, we obtain  $\Sigma_c(\omega) \sim A \frac{\gamma}{\omega - \omega_0 + i\gamma}$ . In addition, we observe a  $\sqrt{|\omega|}$  behavior in the low energy limit as shown in Fig. S2A. Such a dependence fully captures the asymptotic low-energy behavior for the two-channel Kondo model (21, 25). Combining both contributions, we have the form of the self-energy given in the previous section (Eq. S7).

As shown in Fig. S4A, we fit the imaginary part of the self-energy with this form. The Heaviside step function has been replaced by a soft cutoff via a hyperbolic tangent function in the fitting. In Fig. S4B, we also plot the evolution of  $\gamma$ , which characterize the width of the peak, as a function of temperature. At low temperature, we find that  $\gamma$  saturates to a finite value

at a fraction of  $T_K$ . This saturation further supports the robustness of the pole in the complex plane.

Physically, the Kondo effect always leads to the development of  $f$ -electron spectral weight within an energy range of  $T_K$  near the Fermi energy. In the single-channel Kondo/Anderson lattice, such spectral weight is carried by Landau quasiparticles; a pole in  $\Sigma_c(\omega)$  develops whose decay rate must satisfy the Fermi liquid form and depends on  $\omega$  in an  $\omega^2$  form (where  $\omega$  is measured from the Fermi energy). By contrast, in the two-channel Kondo/Anderson lattice model, the  $f$ -electron state can decay into the fractionalized (Majorana) excitations. Consequently, the damping rate  $\gamma$  remains nonzero even at the zero-temperature and zero-frequency limit.

The existence of a pole in the self-energy leads to a band reconstruction in the interacting model, as shown in Fig. S6. Combining the self-energy and symmetry group, we are able to analyze the structure of the Green's function near the Dirac and Weyl nodes.

To further explicate the consequence of the pole in the self-energy, we stress that emergent excitations develop at low energies (within the Kondo scale near the Fermi energy) out of this pole. They take the form of hybridized bands, except that these are not quasiparticles. Specifically, in the vicinity of the crossing wave vector  $\tilde{k}$ , we have

$$\tilde{P}G_c^{-1}(\omega, \tilde{k} + k)\tilde{P} \approx U^\dagger \begin{bmatrix} \omega - E_0 - v_z k_z - \Sigma_c(\omega) & -v_x k_x + i v_y k_y \\ -v_x k_x - i v_y k_y & \omega - E_0 + v_z k_z - \Sigma_c(\omega) \end{bmatrix} U$$

where  $\tilde{P}$  is the projection matrix that only keeps the relevant bands,  $U$  is a unitary matrix that brings the dispersion near a Weyl/Dirac node into the canonical form and  $E_0$  is the energy of the noninteracting Weyl/Dirac nodes.

Importantly, a pole of  $\Sigma_c(\omega)$  in the complex-frequency plane leads to a *doubling* of the bands, creating dispersive modes within the Kondo energy  $T_K$  near the Fermi energy that are not quasiparticles. We illustrate this explicitly for the case of Dirac nodes in 2D, where we can set  $v_z = 0$  and keep implicit the two-fold degeneracy in spin space. The corresponding spectral

functions would have *low-energy* peaks at

$$\omega \approx \omega_0 + \gamma \frac{A}{E_0} (1 \pm \sqrt{v_x^2 k_x^2 + v_y^2 k_y^2 + v_z^2 k_z^2 / E_0}) \quad (\text{S8})$$

We re-iterate that this equation describes the *emergent* dispersive modes located near Fermi energy. The results are shown in Fig. 7A,B,C. The corresponding results for the 3D kagome lattice have already been shown in the main text, Fig. 2A,B,C.

Recognizing that both  $E_0$  and  $A$  are non-universal and generically of the order of the bare conduction electron bandwidth  $D$ , and  $\gamma$  is of the order of  $T_K$ , the velocity of the emergent Weyl nodal states is renormalized down from its noninteracting counterpart by a factor of  $\sim (T_K/D)$ . Each peak corresponds to one branch of the Dirac/Weyl node in the non-Fermi liquid dispersive modes.

In the broad energy range, the pole in the self-energy essentially leads to a band reconstruction in the interacting model, as shown in Fig. S6A,B. The corresponding results for the 3D kagome lattice are shown in Fig. S6C,D.

## G. Topological Dirac semimetal without quasiparticles in the 2D model

The Dirac spectrum appearing near the Fermi energy, for the case of the 2D kagome lattice, is shown in Fig. S7 A,B,C. The emergent dispersive modes near the Fermi energy form a symmetry-protected Dirac node at the  $K$  point. The non-Fermi liquid properties in the 2D kagome lattice are also characterized by the  $\sqrt{T}$  dependence in both the resistivity and valley Hall conductivity, as shown in Fig. S7 D,E.

## H. Symmetry of Green's function in the microscopic models

Based on the eigenvectors and eigenvalues of the single-particle Green's function, we now prove that the Weyl (Dirac) nodes in the 3D kagome model and the Dirac nodes in the 2D kagome

model are both protected by crystalline symmetry, but via different mechanisms. Since single-particle excitations are composite fermions, it is adequate to focus on the Green's function of the  $d$  electrons,  $G_d$ .

The Weyl nodes in 3D kagome model come from the band inversion mechanism. Along the high symmetry line  $K-H$ , we can assign an eigenvalue of  $C_{3z}$  to each dispersive mode (eigenvectors of Green's function). In Fig. 2A, two modes with left-moving and right-moving peaks have symmetry eigenvalues  $\eta^3$  and  $\eta^5$ , respectively. The different eigenvalues would protect the crossing of the two modes under symmetry-preserved perturbations. A similar mechanism protects the Weyl nodes on  $-H-K'-H'$  and Dirac nodes on  $-A-\Gamma-A$ .

In the 2D kagome lattice, the Dirac nodes are symmetry enforced.  $\{v_{d,i}(\omega, \mathbf{k} = K/K')\}_i$  forms the  $\Gamma_1 \oplus \Gamma_3$  representation of the little group  $G_{K/K'} = C_{3v}$ . Due to the  $SU(2)$  symmetry, we can ignore the spin index and use a spinless representation here. The two-dimensional irreducible representation  $\Gamma_3$  enforces a two-fold-degenerate (four-fold-degenerate including the spin degree of freedom) spectrum at the  $K/K'$  point. Consequently, the two dispersive modes have to coincide with each other at the  $K/K'$  point as shown in Fig. S7A.

## I. Edge modes

To evaluate the edge mode in the 3D kagome model, we take a slab geometry with 50 unit cells and open boundary along  $y$  direction. In the interacting model, we consider the Green's function  $[G_d(\omega, k_x, k_z)]_{y_1\alpha_1, y_2\alpha_2}$  that is a  $300 \times 300$  matrix, where  $y_i$  is the coordination of unit-cell along the  $y$  direction and  $\alpha_i$  is the sublattice and spin index. Through diagonalizing the Green's function matrix, we obtain the eigenvalues  $\{g_i(\omega, k_x, k_z)\}_i$  and eigenvectors  $\{[v_i(\omega, k_x, k_z)]_{y\alpha}\}_i$ . For a local self-energy,  $[v_i(\omega, k_x, k_z)]_{y\alpha}$  becomes  $\omega$  independent and describes the real-space distribution of the corresponding mode. Numerically, we identify an edge mode that decays exponentially in the real space as shown in Fig. S8A. The corresponding

spectral function  $\text{Im}[g_i(\omega, k_x, k_z)]/\pi$  is shown in the main text, Fig. 3A.

## J. Hall conductivities

In this section, we describe the calculation of the spin and valley Hall conductivities. Within the DMFT approach, in which vertex corrections are formally suppressed, the in-plane spin Hall conductivity of each  $k_z$ :  $\sigma^s(k_z)$ , can be expressed as

$$\sigma_{xy}^s(k_z) = \frac{1}{4\pi^2} \int_{k_x, k_y} \sum_{m, n \in \uparrow} \tilde{\Omega}_{mn}(k_x, k_y, k_z) - \frac{1}{4\pi^2} \int_{k_x, k_y} \sum_{m, n \in \downarrow} \tilde{\Omega}_{mn}(k_x, k_y, k_z) \quad (\text{S9})$$

where  $m, n$  are band indices. The first (second) terms sum over bands with spin up (down). The full bulk contribution is obtained via  $\sigma_{xy}^s = \int_{k_z} \sigma_{xy}^s(k_z)$ . In addition,

$$\begin{aligned} \tilde{\Omega}_{mn}(\mathbf{k}) &= i \lim_{\nu \rightarrow 0} \frac{d}{d(i\nu)} \frac{1}{\beta} \sum_{i\omega} \frac{(V_{\mathbf{k}}^\dagger \partial_{k^x} t_{\mathbf{k}} V_{\mathbf{k}})_{nm} (V_{\mathbf{k}}^\dagger \partial_{k^y} t_{\mathbf{k}} V_{\mathbf{k}})_{mn}}{[i\omega + i\nu - \epsilon_{\mathbf{k}, n} - \Sigma_c(i\omega)][i\omega - \epsilon_{\mathbf{k}, m} - \Sigma_c(i\omega)]} \\ &= i \lim_{\nu \rightarrow 0} \frac{d}{d(i\nu)} \frac{1}{\beta} \sum_{i\omega} \frac{[A_{\mathbf{k}, mn}^x A_{\mathbf{k}, nm}^y - A_{\mathbf{k}, nm}^x A_{\mathbf{k}, mn}^y] (\epsilon_{\mathbf{k}, n} - \epsilon_{\mathbf{k}, m})^2}{[i\omega + i\nu - \epsilon_{\mathbf{k}, n} - \Sigma_c(i\omega)][i\omega - \epsilon_{\mathbf{k}, m} - \Sigma_c(i\omega)]}. \end{aligned}$$

$V_{\mathbf{k}}, \{\epsilon_{\mathbf{k}, n}\}_n$  are the eigenvectors and eigenvalues (*i.e.* the Bloch bands) of the hopping matrix  $t_{\mathbf{k}}$ .  $A_{mn, \mathbf{k}}^\mu = i \langle u_{m, \mathbf{k}} | \partial_{k^\mu} | u_{n, \mathbf{k}} \rangle$  is a Berry connection.

Similarly, we calculate valley Hall conductivity  $\sigma^\nu$  of 2D kagome lattice via

$$\sigma^\nu = \frac{1}{4\pi^2} \int_{|\mathbf{k}-K| < C} \sum_{m, n} \tilde{\Omega}_{mn}(\mathbf{k}) - \frac{1}{4\pi^2} \int_{|\mathbf{k}-K'| < C} \sum_{m, n} \tilde{\Omega}_{mn}(\mathbf{k}), \quad (\text{S10})$$

where the  $\mathbf{k}$  integration is taken in a finite region near  $K/K'$  with cutoff  $C = \pi/2$ . In the calculation, we introduce a small mass term to the Dirac point in order to generate a finite Berry curvature distribution. From top to bottom, we label the bands by 1, 2, 3. In the noninteracting limit, the lowest band that is below the Fermi energy contributes a positive  $\sigma^\nu$ . The top two bands are above the Fermi energy near  $K(K')$  and, thus the corresponding contributions  $\tilde{\Omega}_{12}$  and  $\tilde{\Omega}_{21}$  vanish. Once we turn on the hybridization  $V$ , dispersive modes develop near the Fermi

energy and generate nonzero  $\tilde{\Omega}_{12}$  and  $\tilde{\Omega}_{21}$ . We can extract the contributions from  $\tilde{\Omega}_{12}$  and  $\tilde{\Omega}_{21}$  and define  $\sigma'_{12}$

$$\sigma'_{12} = \frac{1}{4\pi^2} \int_{|\mathbf{k}-\mathbf{K}|<\Lambda} (\tilde{\Omega}_{12}(\mathbf{k}) + \tilde{\Omega}_{21}(\mathbf{k})) - \frac{1}{4\pi^2} \int_{|\mathbf{k}-\mathbf{K}'|<\Lambda} (\tilde{\Omega}_{12}(\mathbf{k}) + \tilde{\Omega}_{21}(\mathbf{k})).$$

$\sigma'_{12}$  is part of  $\sigma^\nu$  that is directly generated by the interactions. The evolution of  $\sigma^\nu$  and  $\sigma'_{12}$  as a function of hybridization is shown in Fig. S8B.

## K. Non-linear Hall effect

We now turn to the non-linear Hall effect in the non-Fermi liquid phase. Using the Green's function approach (49), the non-linear Hall conductivity is

$$\begin{aligned} \chi_{xyy} = & -\frac{1}{2\pi} \int_{\mathbf{k}, \epsilon} \text{Im} \left\{ \text{Tr} \left[ \partial_\epsilon f(\epsilon) u_x \partial_\epsilon G_c(\epsilon - i0^+) u_y G_c(\epsilon - i0^+) u_y G_c(\epsilon + i0^+) \right. \right. \\ & + \partial_\epsilon f(\epsilon) u_x \partial_\epsilon G_c(\epsilon - i0^+) u_{yy} G_c(\epsilon + i0^+) + f(\epsilon) u_x \partial_\epsilon^2 G_c(\epsilon - i0^+) u_{yy} \\ & \left. \left. + 2f(\epsilon) u_x \partial_\epsilon [G_c(\epsilon - i0^+) u_y G_c(\epsilon - i0^+)] u_y G_c(\epsilon + i0^+) \right] \right\}, \end{aligned} \quad (\text{S11})$$

where  $f(\epsilon)$  is the Fermi-Dirac function, and  $u_{\mu_1 \mu_2 \dots \mu_n} = \partial_{k_{\mu_1} k_{\mu_2} \dots k_{\mu_n}} t_{\mathbf{k}}$ . Each term contains a product of three Green's functions with two derivatives of  $\epsilon$ . In the asymptotic region  $c_{IR} < \omega \ll T_K$  where scaling behaviors appear,  $G_c(\epsilon) \sim g_0 + g_1 \sqrt{|\epsilon|}$ .  $c_{IR}$  acts as an infrared cutoff. The integral behaves as  $\sim \epsilon^{-3/2} d\epsilon$ . (Note that at least one derivative is acting on the Green's function.) Transforming to the temperature behaviors, we would expect  $\sim 1/\sqrt{T}$  in the scaling region  $c_{IR} < T \ll T_K$ . To more explicitly observe this  $\sim 1/\sqrt{T}$  behaviors, we consider the Green's function near the Weyl node  $\tilde{\mathbf{k}}$

$$G_c(\omega, \mathbf{k} + \tilde{\mathbf{k}})^{-1} \approx [\omega - h_0 - \Sigma_c(\omega)] \mathbb{I} - h_x \sigma^x - h_y \sigma^y - h_z \sigma^z,$$

where  $\Sigma_c(\omega)$  is the self-energy.  $\sigma^{x,y,z}$  are Pauli matrices in the  $2 \times 2$  subspace that holds the Weyl node.  $h_0, h_x, h_y, h_z$  are functions of wave vector. At the Weyl node,  $h_0(\tilde{\mathbf{k}}) = E_0$ ,  $h_x(\tilde{\mathbf{k}}) =$



$h_y(\tilde{\mathbf{k}}) = h_z(\tilde{\mathbf{k}}) = 0$ . The eigenvalues of the Green's function matrix are

$$g_{\pm}^{-1} = \omega - \epsilon_{\pm} - \Sigma_c(\omega)$$

$$\epsilon_{\pm} = h_0 \pm \sqrt{h_x^2 + h_y^2 + h_z^2},$$

where  $\Sigma_c(\omega)$  is the self-energy and has non-Fermi liquid behavior. We also introduce the velocity matrix:  $v_{\mu}^{\alpha\gamma} = (V^{\dagger} \partial_{k^{\mu}} t_{\mathbf{k}} V)_{\alpha\gamma}$ , where  $t_{\mathbf{k}} = h_0 \mathbb{1} + h_x \sigma^x + h_y \sigma^y + h_z \sigma^z$  is the hopping matrix and  $V$  is the matrix formed by the eigenvectors of the hopping matrix.

Here, we focus on the intrinsic contributions from the Berry curvature (50). However, all the other contributions produce the same  $1/\sqrt{T}$  behavior. The intrinsic contributions reads (from the first term of Eq. S11),

$$\chi_{xyy}^{in} = -\frac{1}{2\pi} \int_{\mathbf{k}} \int d\epsilon \frac{\partial f(\epsilon)}{\partial \epsilon} \text{Im} \left\{ \text{Tr} \left[ \begin{aligned} & v_x^{+-} v_y^{-+} v_y^{++} \partial_{\epsilon} g_{-}(\epsilon + i0^+) g_{+}(\epsilon + i0^+) g_{+}(\epsilon - i0^+) \\ & + v_x^{-+} v_y^{++} v_y^{+-} \partial_{\epsilon} g_{+}(\epsilon + i0^+) g_{+}(\epsilon + i0^+) g_{-}(\epsilon - i0^+) \end{aligned} \right] \right\}.$$

Due to the pre-factor  $\frac{\partial f(\epsilon)}{\partial \epsilon}$ , it is sufficient to focus on the low-energy contribution. Since the self-energy behaves as  $\text{Im}[\Sigma_c] \sim a + b\sqrt{|\omega|}$ , approximately we have

$$\chi_{xyy}^{in} = -\frac{1}{2\pi} \int_{\mathbf{k}} \int_{\epsilon} \frac{\partial f(\epsilon)}{\partial \epsilon} \Omega_{xy}^{+} v_y^{++} \left[ a_0 + \frac{a_1}{\sqrt{|\epsilon|}} + o(\epsilon) \right]$$

where  $a_1 \approx \pi(\rho_0 \frac{\sqrt{h_x^2 + h_y^2 + h_z^2}}{h_0})^3 \frac{1}{\sqrt{\Lambda}}$  and  $\Lambda$  is the low energy scale of  $\sqrt{|\omega|}$  behaviors and  $\rho_0$  is the density of state near zero Fermi energy. After integrating over  $\epsilon$ , we have

$$\chi_{xyy}^{in} = \frac{1}{\sqrt{T}} \cdot \left[ \frac{-1.34}{2\pi} \int_{\mathbf{k}} \Omega_{xy}^{+} v_y^{++} a_1 \right] + \dots \quad (\text{S12})$$

where  $\Omega_{xy}^{+} = i\langle \partial_x u_+ | \partial_y u_+ \rangle - i\langle \partial_y u_+ | \partial_x u_+ \rangle$  is the Berry curvature.

## L. Candidate materials

We have identified three candidate materials, PrBi (26, 51, 52), PrFe<sub>4</sub>P<sub>12</sub> (27, 53), and UPT<sub>3</sub>Au<sub>2</sub> (28), to realize the correlated topological phases predicted here. They crystallize in the space

groups #225, #204, and #216, respectively, which all allow for a  $\Gamma_3$  non-Kramers doublet ground state of the  $\text{Pr}^{3+}$  or  $\text{U}^{4+} 4f^2$  wave function. The former two are centrosymmetric and candidate correlated Dirac semimetals, whereas the latter is noncentrosymmetric and thus a candidate correlated Weyl semimetal.

In PrBi, evidence for a  $\Gamma_3$  ground state was provided by fitting a crystal electric field (CEF) model to temperature-dependent magnetic susceptibility data; the assignment was supported by a much better agreement of the specific heat data with this than other possible CEF level schemes (26). A low charge carrier concentration was evidenced from quantum oscillation experiments (26). For  $\text{PrFe}_4\text{P}_{12}$ , key evidence is summarized in Fig. S9. A non-magnetic CEF ground state doublet is suggested by the antiferroquadrupolar ordering at low temperatures (panel A) (27). Strong Kondo coupling was evidenced by a large Sommerfeld coefficient determined from specific heat data (54), and is confirmed by the large  $A$  coefficient of the Fermi liquid  $T^2$  form seen in electrical resistivity data under applied pressure and magnetic field (inset of panel B). Under finite pressure, the material shows an upturn of the electrical resistivity with decreasing temperature, *i.e.*, it ceases to be metallic. We thus anticipate that  $\text{PrFe}_4\text{P}_{12}$  under finite pressure and PrBi under ambient pressure may fulfill the theoretical requirements for topological two-channel Kondo systems. Finally,  $\text{UPt}_3\text{Au}_2$  shows a moderately enhanced Sommerfeld coefficient of  $60 \text{ mJ/mol/K}^2$ , and an only very weakly temperature-dependent electrical resistivity (28) (see Fig. S10), that may point to the presence of Kondo interaction in a reduced carrier concentration setting.

## **M. Space group symmetry constraints in the candidate materials**

As discussed in the main text, PrBi (26, 51) and  $\text{PrFe}_4\text{P}_{12}$  (27, 53) have space groups #225 and #204, respectively. Whereas  $\text{UPt}_3\text{Au}_2$  (28), which has a broken inversion symmetry, has space group #216. These space groups allow for Dirac or Weyl points. For example, in PrBi, if two

bands with the crossing point on the  $\Gamma$ - $X$  line have different eigenvalues under the  $4_{100}^+$  rotational symmetry, it would be a symmetry-protected Dirac node; this symmetry-based argument is manifested in the DFT calculations (albeit without treating correlation effects), in which a band crossing occurs on the  $\Gamma$ - $X$  line (51). Similarly, the  $3_{111}^+$  rotational symmetry could protect Dirac nodes on the  $\Gamma$ - $H$  line in  $\text{PrFe}_4\text{P}_{12}$ . Likewise, the  $2_{100}$  rotational symmetry could protect Weyl nodes on the  $X$ - $W$  line of  $\text{UPt}_3\text{Au}_2$ .

## **N. DFT calculations**

The theoretical electronic-structure calculations for  $\text{PrBi}$  were carried out using the Vienna ab initio simulation package (VASP) (55, 56) with the modified Becke-Johnson potential (57, 58) for the generalized gradient approximation of the exchange-correlation functional. The pseudo-potentials in the projector augmented-wave approximation (59) included  $p$  and  $s$  valence electrons for Bi atoms, while for Pr the  $f$  electrons were frozen in the core. The spin-orbit interaction was also considered in the calculation by the second variation method (60). The self-consistent calculation of the ground state density was performed in a  $11 \times 11 \times 11$  Monkhorst-Pack grid with an energy cutoff of 600 eV.

## Supplementary Figures

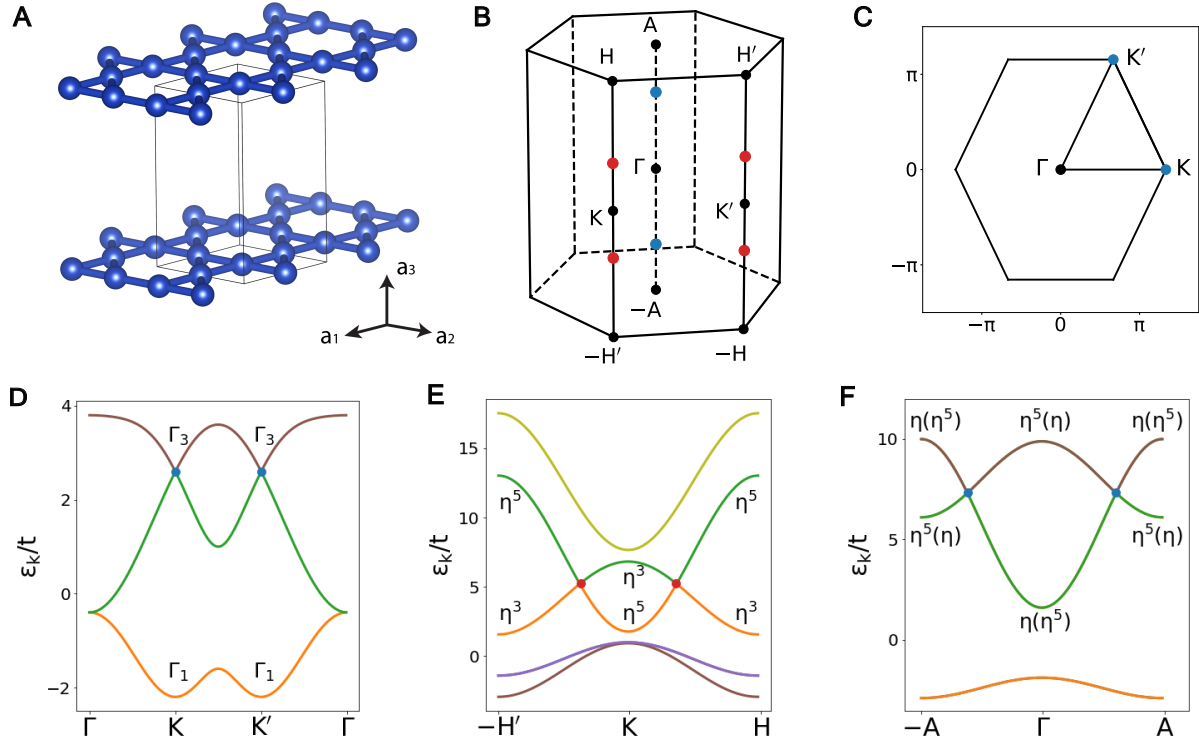


Figure S1: **Lattice structure and the noninteracting dispersion.** (A) The 3D kagome lattice. (B) The first Brillouin zone of the 3D kagome lattice, where red and blue dots denote the Weyl nodes and Dirac nodes, respectively. (C) The first Brillouin zone of the 2D kagome lattice, where the blue dots denote the Dirac nodes. (D) Dispersion of the 2D kagome lattice. (E), (F) Dispersion of the 3D kagome lattice along two high-symmetry lines of the Brillouin zone. Here 0 marks the Fermi energy of the conduction electrons in the absence of the Kondo hybridization. The relevant bands are marked by their eigenvalues of the  $C_{3z}$  symmetry, where  $\eta = e^{i2\pi/6}$ .

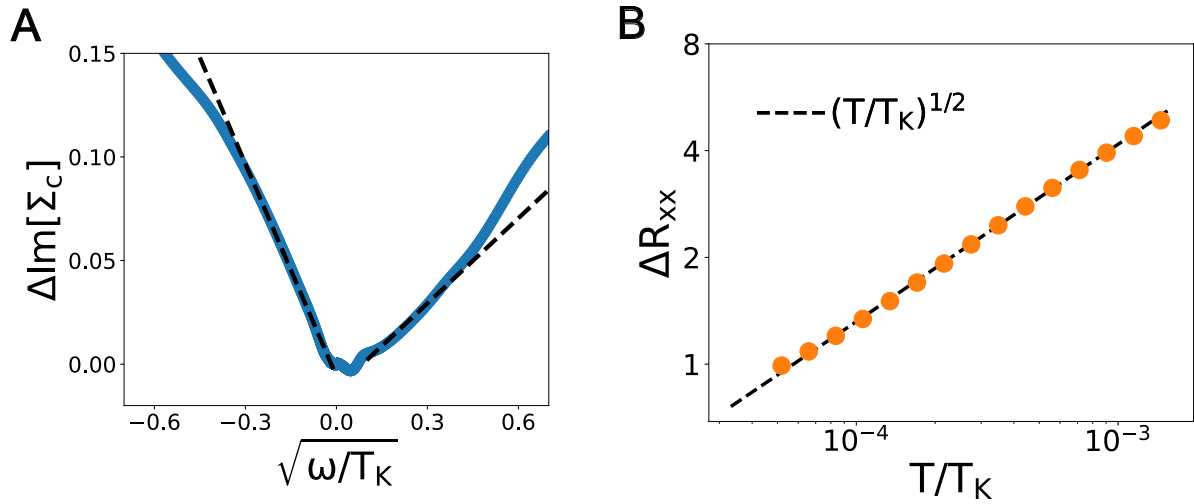


Figure S2: **Breakdown of Landau quasiparticles.** (A) The self-energy ( $\Sigma_c$ ) shows a  $\sqrt{|\omega|}$ -dependence at low temperatures (shown here for  $T/T_K = 10^{-3}$ ) in the 3D kagome lattice. To isolate the frequency dependence, the zero frequency contribution has been subtracted in the plot:  $\Delta\text{Im}[\Sigma_c](\omega) = \text{Im}[\Sigma_c](\omega) - \text{Im}[\Sigma_c](0)$ . (B) Temperature dependence of the electrical resistivity along the  $x$  direction in the 3D kagome lattice. Both the  $\sqrt{|\omega|}$  and  $\sqrt{T}$  dependencies characterize the breakdown of quasiparticles.

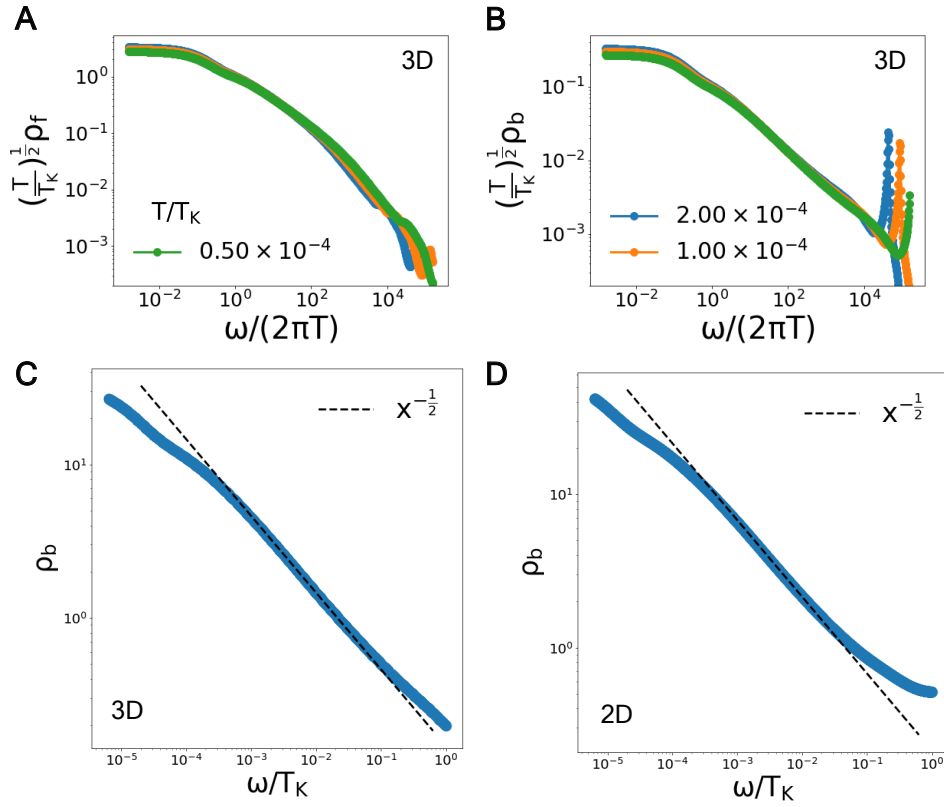


Figure S3: **Dynamical scaling and power-law behavior.** (A), (B) spectral functions of  $\rho_f$  and  $\rho_b$  in the 3D kagome lattice at various temperatures in unit of  $T_K$ . (C) and (D) show the power-law dependence of the pseudo-particle spectral functions for the models on the 3D and 2D kagome lattices, respectively. The spectral function  $\rho_b$  is shown to depend on frequency in a power-law form,  $\omega^{-1/2}$ . The power-law form operates for about two decades of frequency. The deviation at high frequencies captures the effect of the ultraviolet energy cutoff. That at low frequencies reflects a nonzero (albeit very low) temperature where the calculation is performed ( $T = 4 \times 10^{-5} T_K$ ).

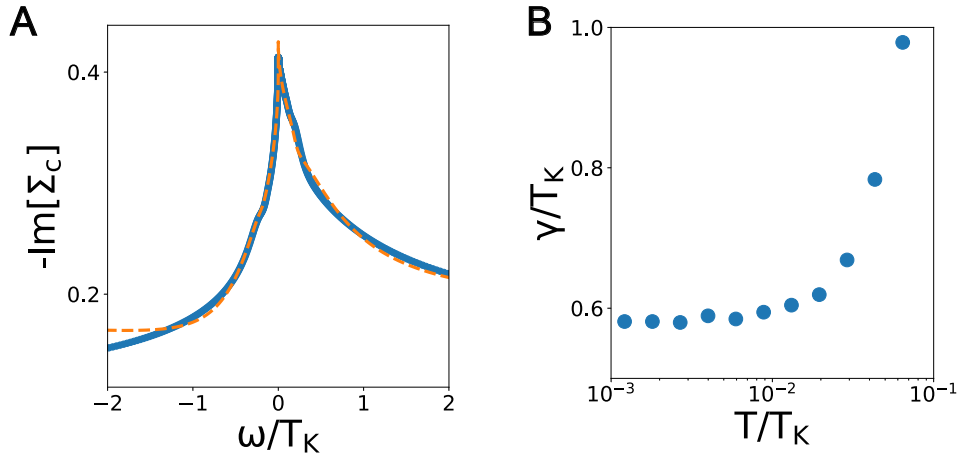


Figure S4: **Emergence of a pole in the self-energy.** Fitting of the self-energy using Eq. S7. Note that  $g(\omega)$ , which describes the asymptotic behavior of the self-energy, takes the form  $a + c\sqrt{|\omega|}$ . The blue solid line shows the imaginary part of the self-energy calculated in the 3D kagome lattice at  $T/T_K = 10^{-3}$ . The orange dash line is the fitted curve. We observe a good consistency between the two. **(B)** Evolution of the fitted width  $\gamma$  as a function of temperature in the 3D kagome lattice. It saturates to a nonzero value at temperatures low compared to  $T_K$ .

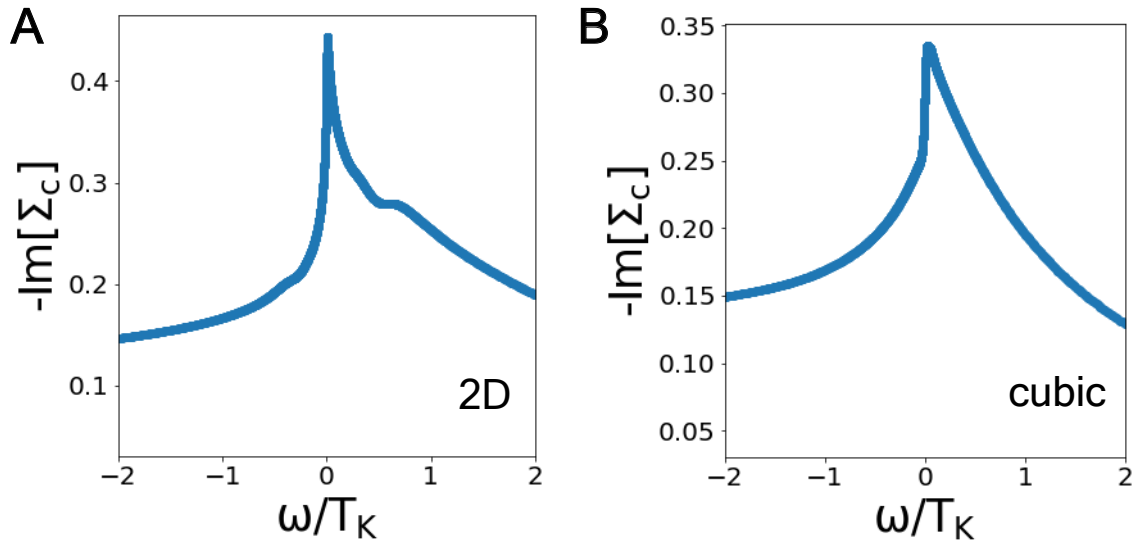


Figure S5: **The imaginary part of the self-energy.** Shown are the results for the 2D kagome lattice (A) and cubic lattice (B). The calculations are done at the temperature  $T/T_K = 10^{-3}$  in both cases.



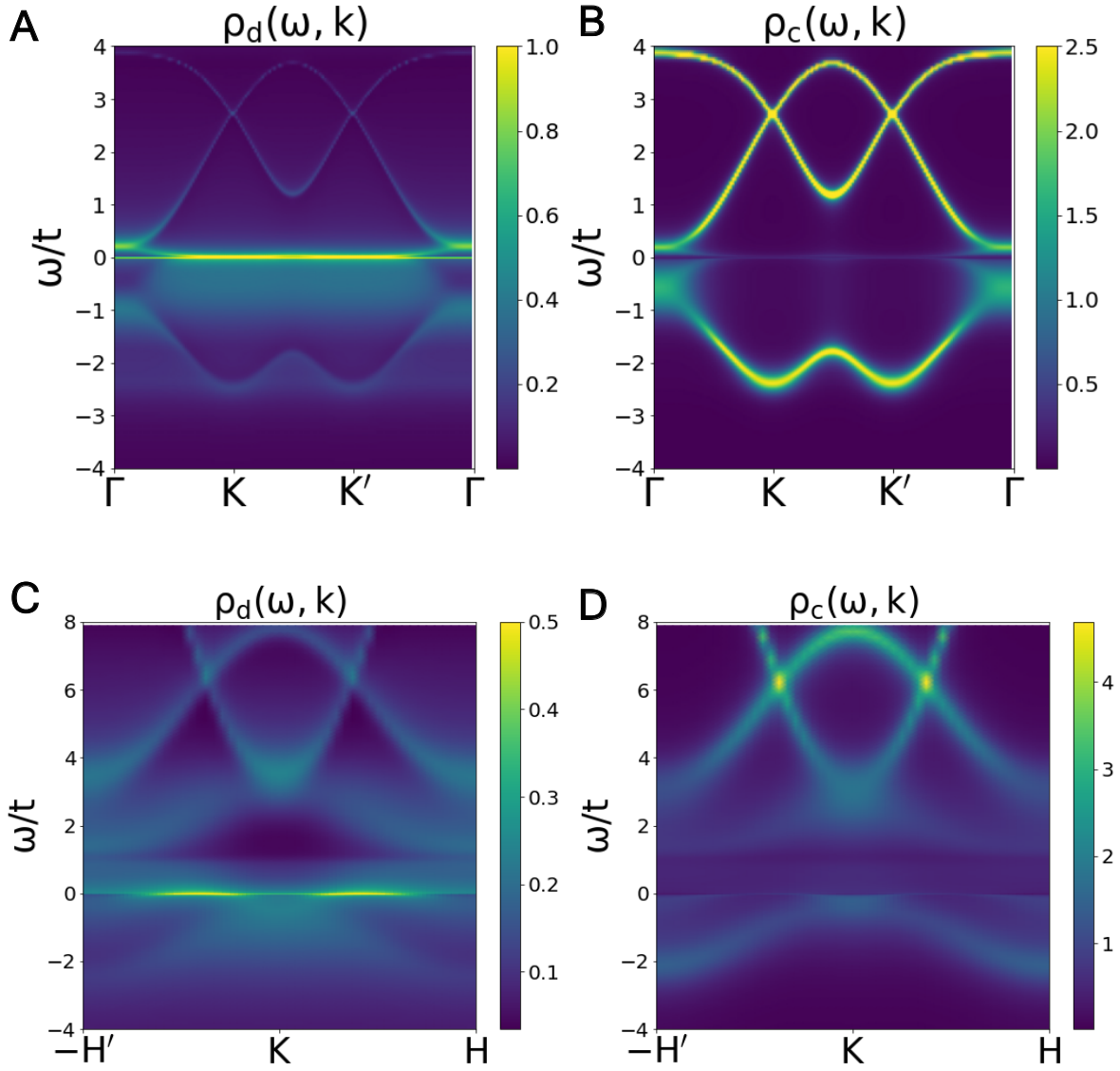


Figure S6: **Band reconstruction from the self-energy pole.** (A) and (B) show the spectral functions of the  $d$  and  $c$  electrons in the 2D kagome lattice. (C) and (D) show the corresponding results in the 3D kagome lattice. All calculations are done at  $T/T_K = 10^{-3}$ . We can observe band reconstruction near the Fermi energy in both cases.

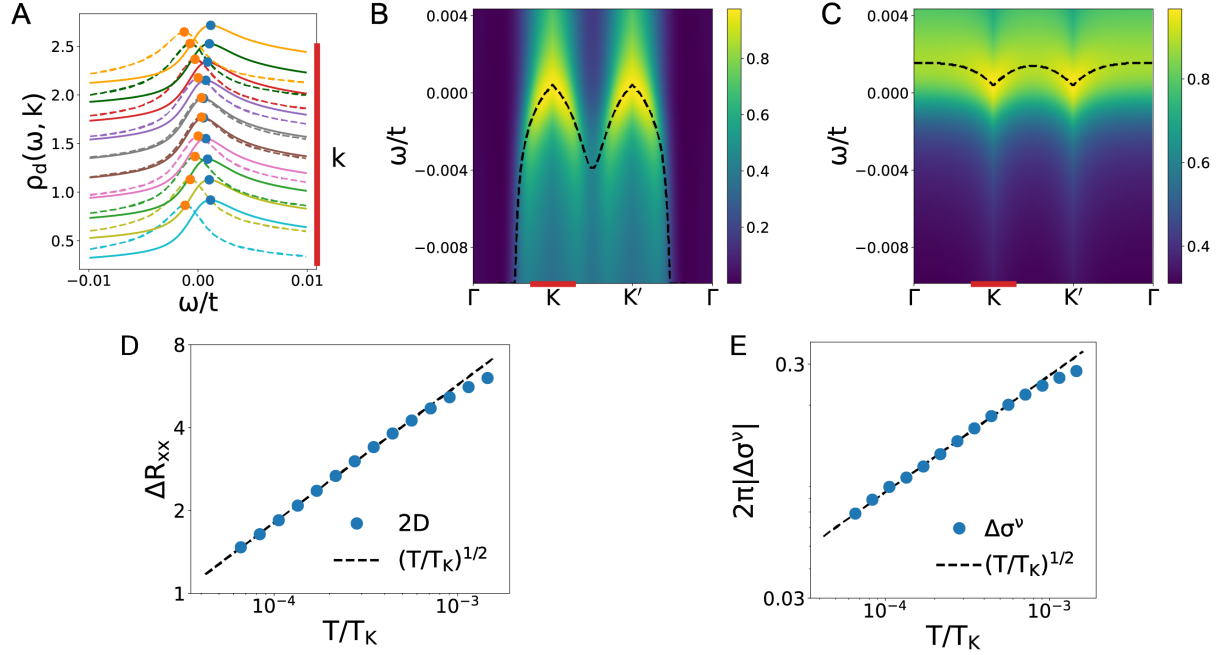


Figure S7: **Emergence of non-Fermi liquid Dirac nodal excitations in the 2D model.** (A) The  $d$  electron spectral functions ( $\rho_d$ ) at various  $k$  points (marked by the red bar on the right) along high symmetry line in the 2D kagome lattice. Solid and dashed lines denote two dispersive modes from two eigenvalues of the Green's function. The blue and orange dots label the positions of the spectral peaks, which meet at a Dirac point. Each  $\rho_d$  curve has been shifted vertically to avoid overlapping. (B),(C) illustrate the spectral functions of the two Dirac-point-bearing branches. Here, the dashed line denotes the energy spectral peaks. The red bar marks the cut of wave vectors in the Brillouin zone along which the spectral functions are shown in panel A. The calculations are done at the temperature  $T/T_K = 10^{-3}$  in all cases. Temperature dependence of the electrical resistivity along the  $x$  direction (D) and valley Hall conductivity (E). Both quantities depend on temperature in a  $\sqrt{T}$  manner.

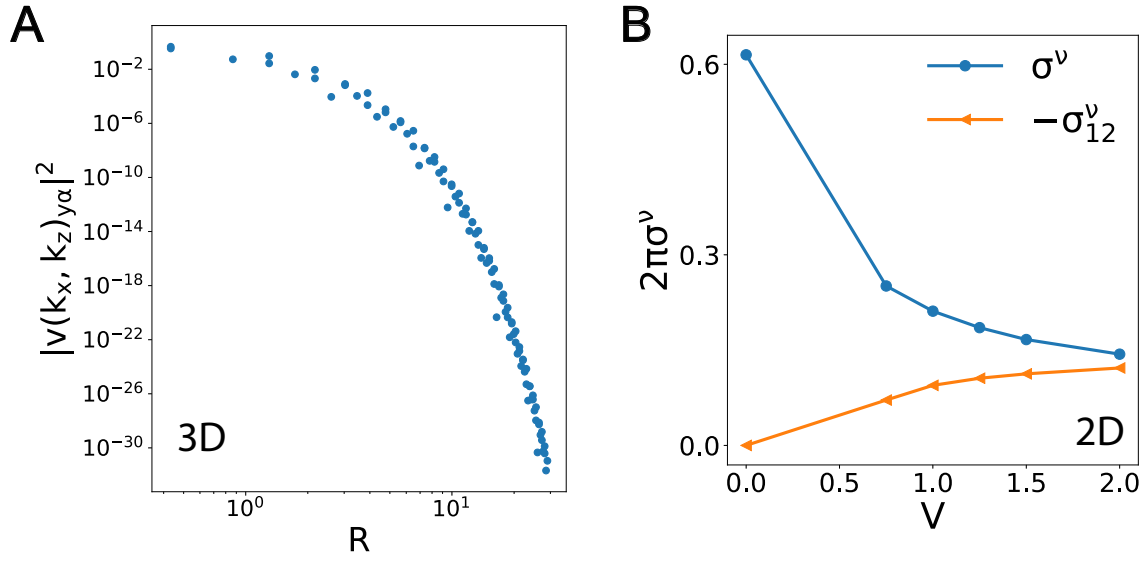


Figure S8: **Edge state and the valley Hall effect.** (A) Exponential decay of the edge-mode eigenvector  $v(k_x = 4\pi/3, k_z = 0)_{\alpha y}$  in the 3D kagome model.  $R$  denotes the distance to the edge. (B) Valley Hall conductivity as a function of  $V$  in the 2D kagome model with fixed  $V/\epsilon_f = -0.5$  at  $T/T_K = 10^{-3}$ .

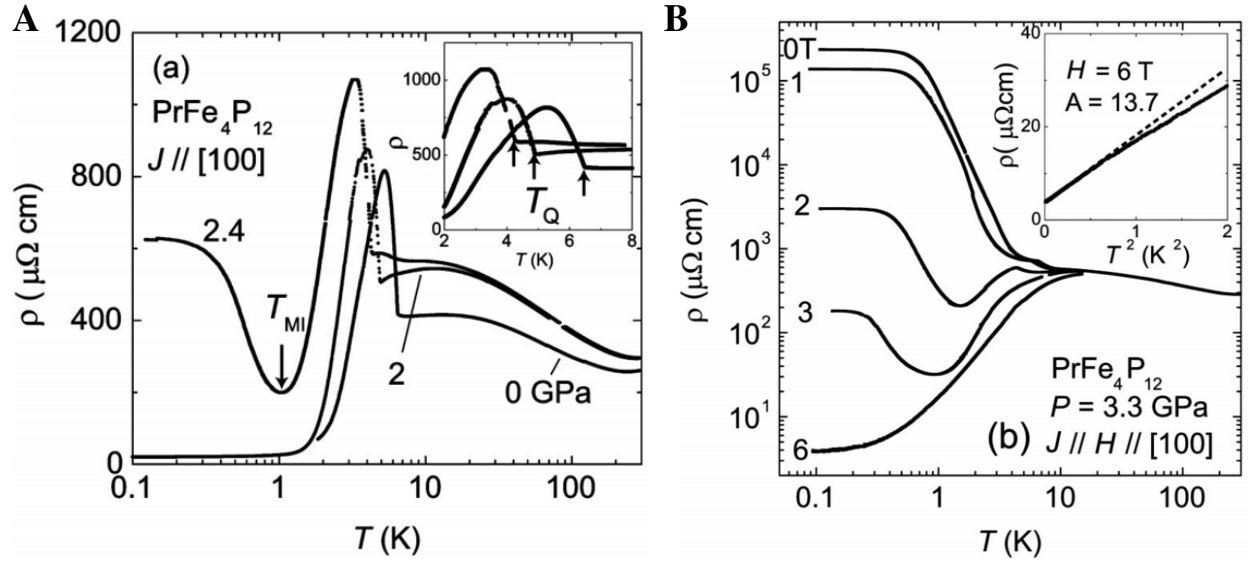


Figure S9: **Candidate two-channel Kondo material  $\text{PrFe}_4\text{P}_{12}$ .** (A) Temperature-dependent electrical resistivity at ambient pressure and at 2 GPa and 2.4 GPa, revealing that the transition temperature  $T_Q$  of the phase with antiferroquadrupolar order is successively suppressed with increasing pressure (see inset). At lower temperatures, a resistivity upturn is observed below  $T_{\text{MI}}$ . (B) Temperature-dependent electrical resistivity at 3.3 GPa, for several fixed magnetic fields up to 6 T. The non-metallic state is readily suppressed by magnetic field. At 6 T,  $\text{PrFe}_4\text{P}_{12}$  has metallized and exhibits heavy fermion behavior, as evidenced by the strongly enhanced  $T^2$  prefactor  $A = 13.7 \mu\Omega\text{cm}/\text{K}^2$  which, assuming the validity of the Kadowaki-Woods relation, corresponds to a Sommerfeld coefficient of about  $1 \text{ J/mol}/\text{K}^2$ , in good agreement with specific heat experiments (54). From Ref. 27.

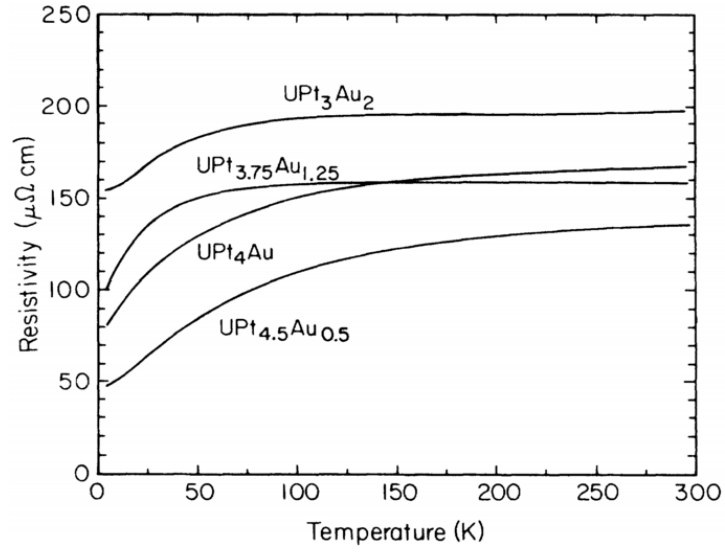


Figure S10: **Candidate two-channel Kondo material  $\text{UPt}_3\text{Au}_2$ .** (A) Temperature-dependent electrical resistivity for several  $\text{UPt}_{5-x}\text{Au}_x$  samples. The weak temperature dependence of  $\text{UPt}_3\text{Au}_2$ , together with the large resistivity values at low temperatures, suggests that it is not metallic. From Ref. 28.

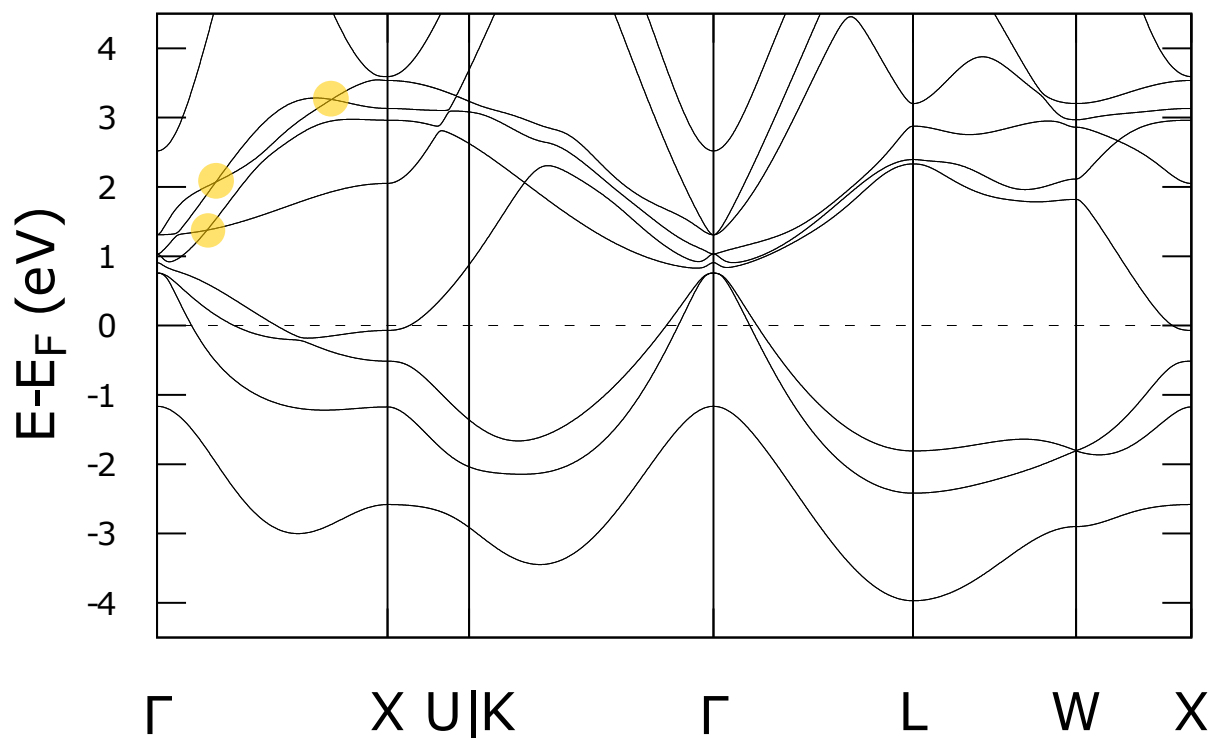


Figure S11: **DFT results in PrBi.** The bandstructure of the *spd* conduction electrons of PrBi, from *f*-core DFT calculations. The three yellow dots mark the Dirac points. The Dirac points in the non-*f* conduction electron states appear far away from the Fermi energy, and support the lattice symmetry argument given in this SM, Sec. M.